

## MISR Calibration and Implications for Low-Light-Level Aerosol Retrieval over Dark Water

RALPH KAHN, WEN-HAO LI, JOHN V. MARTONCHIK, CAROL J. BRUEGGE, DAVID J. DINER,  
BARBARA J. GAITLEY, AND WEDAD ABDOU

*Jet Propulsion Laboratory, California Institute of Technology, Pasadena, California*

OLEG DUBOVIK, BRENT HOLBEN, AND ALEXANDER SMIRNOV

*NASA Goddard Space Flight Center, Greenbelt, Maryland*

ZHONGHAI JIN

*NASA Langley Research Center, Langley, Virginia*

DENNIS CLARK

*NOAA/NESDIS, Camp Springs, Maryland*

(Manuscript received 30 April 2004, in final form 29 June 2004)

### ABSTRACT

Studying aerosols over ocean is one goal of the Multiangle Imaging Spectroradiometer (MISR) and other spaceborne imaging systems. But top-of-atmosphere equivalent reflectance typically falls in the range of 0.03 to 0.12 at midvisible wavelengths and can be below 0.01 in the near-infrared, when an optically thin aerosol layer is viewed over a dark ocean surface. Special attention must be given to radiometric calibration if aerosol optical thickness, and any information about particle microphysical properties, are to be reliably retrieved from such observations. MISR low-light-level vicarious calibration is performed in the vicinity of remote islands hosting Aerosol Robotic Network (AERONET) sun- and sky-scanning radiometers, under low aerosol loading, low wind speed, relatively cloud free conditions. MISR equivalent reflectance is compared with values calculated from a radiative transfer model constrained by coincident, AERONET-retrieved aerosol spectral optical thickness, size distribution, and single scattering albedo, along with in situ wind measurements. Where the nadir view is not in sun glint, MISR equivalent reflectance is also compared with Moderate Resolution Imaging Spectroradiometer (MODIS) reflectance. The authors push the limits of the vicarious calibration method's accuracy, aiming to assess absolute, camera-to-camera, and band-to-band radiometry. Patterns repeated over many well-constrained cases lend confidence to the results, at a few percent accuracy, as do additional vicarious calibration tests performed with multiplatform observations taken during the Chesapeake Lighthouse and Aircraft Measurements for Satellites (CLAMS) campaign. Conclusions are strongest in the red and green bands, but are too uncertain to accept for the near-infrared. MISR nadir-view and MODIS low-light-level absolute reflectances differ by about 4% in the blue and green bands, with MISR reporting higher values. In the red, MISR agrees with MODIS band 14 to better than 2%, whereas MODIS band 1 is significantly lower. Compared to the AERONET-constrained model, the MISR aft-viewing cameras report reflectances too high by several percent in the blue, green, and possibly the red. Better agreement is found in the nadir- and the forward-viewing cameras, especially in the blue and green. When implemented on a trial basis, calibration adjustments indicated by this work remove 40% of a 0.05 bias in retrieved midvisible aerosol optical depth over dark water scenes, produced by the early postlaunch MISR algorithm. A band-to-band correction has already been made to the MISR products, and the remaining calibration adjustments, totaling no more than a few percent, are planned.

### 1. Introduction

The importance of retrieving aerosol optical thickness (AOT) and aerosol properties over dark water first drew attention when it was recognized that mineral

dust from source regions in the Sahara Desert is regularly transported across the Atlantic Ocean and deposited in the Caribbean (reviewed by Prospero et al. 1983). Subsequent measurements identified significant transoceanic material redistribution of Asian dust and pollution as well (e.g., Clarke et al. 2001; Gao et al. 2001). In addition to material transports, the global-scale direct and indirect radiative impact of aerosols cannot be assessed adequately without a good under-

---

*Corresponding author address:* Dr. Ralph Kahn, Jet Propulsion Laboratory, California Institute of Technology, 4800 Oak Grove Drive, Pasadena, CA 91109.  
E-mail: Ralph.Kahn@jpl.nasa.gov

standing of the over-ocean contribution. It is estimated that top-of-atmosphere (TOA) reflected solar radiation flux varies with midvisible optical depth at a rate between 10 and 60  $\text{W m}^{-2}$  per AOT, depending on aerosol type and other environmental attributes (e.g., Penner et al. 1994). To resolve total aerosol direct radiative forcing of a few watts per meters squared over ocean, needed to assess aerosol climate impacts, AOT must be retrieved to an accuracy of about 0.01 or 0.02.

The Multiangle Imaging Spectroradiometer (MISR) is one of a new generation of instruments designed to observe the earth's environment globally (Diner et al. 1998a). The instrument was launched into polar orbit on 18 December 1999, aboard the National Aeronautics and Space Administration (NASA) Earth Observing System (EOS) *Terra* spacecraft. MISR makes near-simultaneous measurements at nine view angles spread out in the forward (f) and aft (a) directions along the flight path, at  $\pm 70.5^\circ$  (cameras Df and Da),  $\pm 60.0^\circ$  (Cf and Ca),  $\pm 45.6^\circ$  (Bf and Ba),  $\pm 26.1^\circ$  (Af and Aa), and nadir (An), in each of four spectral bands centered at 446, 558, 672, and 866 nm. MISR obtains global coverage, to  $\pm 82^\circ$  latitude, about once per week, with a spatial sampling rate as fine as 275 m at all angles. The instrument systematically covers a range of airmass factors from 1 to 3, and in midlatitudes, samples scattering angles extending from about  $60^\circ$  to  $160^\circ$ . Such data can provide greater sensitivity to AOT than single-view measurements, especially over bright surfaces (Martonchik et al. 2004), over land in general (Abdou et al. 2005; Kahn et al. 2005), and for situations where the AOT is very low (Kahn et al. 1998). The data also contain considerable information about particle size and shape, particularly over dark surfaces (Kahn et al. 2001a; Kalashnikova et al. 2005).

However, early postlaunch comparisons between MISR-retrieved midvisible AOT and near-simultaneous, surface-based sun photometer observations reveal a systematic offset: the MISR AOT values are higher by about 0.05, in comparisons for dark water sites globally (Kahn et al. 2005). MISR measurements coordinated with airborne sun photometer observations during the Chesapeake Lighthouse and Aircraft Measurements for Satellites (CLAMS) campaign in summer 2001, under carefully monitored conditions, produce similar results (Redemann et al. 2005). Particle models and other assumptions in the aerosol retrieval algorithm may contribute to the discrepancy, as well as physical differences between the forward-scattering sun photometer and back-scattering satellite observations, and uncertainties in the sun photometer measurements themselves. Evaluating and refining MISR's radiometric calibration are necessary first steps toward understanding these differences and realizing the full potential of the MISR measurements for this application.

Global average midvisible column AOT is near 0.15, and away from source regions and plumes, column

AOT is typically 0.07 or less (e.g., Smirnov et al. 2002; Husar et al. 1997). Over dark surfaces, such small aerosol loading produces TOA equivalent reflectances below 0.07 at midvisible wavelengths. Simulation of an aerosol mixture for which medium, spherical, nonabsorbing particles contribute 75% to the midvisible AOT of 0.05, 15% from black carbon and 10% from cirrus, over dark water, offers a representative case. The equivalent reflectance is 0.05 in the MISR red (672 nm), 0.02 in near-infrared (866 nm) channels for the  $70^\circ$  forward view, and 0.02 and 0.008 for the red and near-infrared bands in the nadir view. To achieve sensitivity to AOT changes of 0.02 for such cases, a radiometer must reliably measure equivalent reflectance to 0.005 or better. (In this paper, we use decimal notation for absolute reflectance and percent for relative reflectance differences.)

Calibrating an orbiting sensor to this accuracy is at the cutting edge of current capabilities and is beyond what could be achieved for previous generations of satellite instruments. Early postlaunch MISR calibration efforts concentrated on higher reflectance levels, using a combination of preflight, onboard, and field vicarious calibration data (Bruegge et al. 1996; Bruegge et al. 1998; Bruegge et al. 2002; Chrien et al. 2002). For low light levels, the early work followed the traditional approach of extrapolating linearly to zero the calibration obtained for 15%–30% equivalent reflectance. The resulting low-light-level absolute calibration uncertainty is reported as about  $\pm 5\%$  (Bruegge et al. 2002).

In this paper we undertake vicarious calibration aimed at characterizing MISR low-light-level radiometric performance in the reflectance range critical for aerosol retrieval over dark water. The challenge of this effort is to reduce comparison-data uncertainties as much as possible, and then to assess their magnitudes fairly. Fifteen events between 2000 and 2002, when MISR acquired data coincident with operating Aerosol Robotic Network (AERONET) surface-based sun-photometer stations, are at the heart of this study. AERONET offers multiple instruments and multiple events, extending over a variety of surface and atmospheric conditions (Holben et al. 1998). The 15 events chosen here cover a range of midvisible AOT from below 0.03 to 0.3 and equivalent reflectance from about 0.02 to 0.08 in the MISR red channel. For a vicarious calibration study, such diversity helps build confidence in the patterns that emerge; to obtain quantitative conclusions, we can afford to select the best-constrained cases, since MISR radiometric performance is very stable (Bruegge et al. 2002). To further test the observed patterns, we also study coincident MISR, AirMISR, and field data taken on 2 days during the CLAMS campaign.

We use AOT, aerosol size distribution, and particle single scattering albedo (SSA) retrieved from AERONET data to constrain simulations of TOA equivalent

reflectance at all nine MISR view angles and four wavelengths and compare the calculated reflectances with corresponding values from the MISR calibrated and georectified radiance product (MISR L1B2, version F03\_0022, is used throughout this paper, available online from the NASA Langley Atmospheric Sciences Data Center at <http://eosweb.larc.nasa.gov/>). We examine band-to-band, camera-to-camera, and absolute radiometric performance. In cases for which the nadir view is not in sun glint, we also compare with coincident reflectances acquired by the multispectral, nadir-viewing Moderate Resolution Imaging Spectroradiometer (MODIS) instrument, which flies on the *Terra* satellite with MISR. These comparisons allow us to establish the MISR reflectance scale to an absolute accuracy of a few percent, in the equivalent reflectance range of interest. A separate paper (Bruegge et al. 2004) summarizes calibration constraints available from MISR preflight, onboard, and lunar calibration analyses, along with additional comparisons between coincident MISR and MODIS scenes.

## 2. MISR and AERONET data

We identified AERONET stations on islands surrounded by dark, Case 1 waters, isolated from continental runoff, and found instances for which there are coincident, high quality AERONET aerosol retrieval results and MISR radiance data. Since this is a calibration exercise, we chose only the best-constrained events in all relevant dimensions. We selected cases having low midvisible column AOT (0.3 or less), low AOT variability based on AERONET time series, low regional near-surface wind speed, and relatively cloud free conditions near the AERONET site (Table 1). We used back trajectories [Hybrid Single-Particle Lagrangian Integrated Trajectory (HYSPLIT) model, 2003] to find cases likely to involve primarily clean maritime aerosols, so aerosol absorption and nonspherical particle shapes are less likely to introduce uncertainties into the modeling. We also collected surface pressure from local sources, and satellite-derived ozone column amount, as model inputs (Table 1).

### a. MISR data processing

For each event, we selected two to four patches over dark water within 28 km of the AERONET site, in cloud-free areas to the north, south, east, and west, if possible (Fig. 1). Each patch is an array of  $3 \times 3$  MISR 1.1-km pixels. We apply stringent constraints to prevent scene variability or sun glint from skewing the vicarious calibration results. To assure patch uniformity, we require that the equivalent reflectance vary less than 0.5% from the mean pixel value of observed equivalent reflectance; this criterion must be met by each angular view that is not sun-glint contaminated, at all wavelengths. Sun-glint contamination is avoided by eliminat-

ing any MISR view that either falls within  $40^\circ$  of the sun's reflection vector from the nominal surface or is near this value and exhibits a patch radiance variance 3 or more times greater than cameras viewing farther from the sun-glint direction.

Patch-average equivalent reflectance was calculated from the MISR standard level 1B2 product, according to

$$\rho_{\text{MISR}}(\lambda, \mu) = L_{\text{MISR}}(\lambda, \mu) \times \pi D^2 / E_0(\lambda). \quad (1)$$

Here,  $\lambda$  indexes the MISR spectral band and  $\mu$  references the cosine of the MISR view angle,  $L_{\text{MISR}}$  is the radiance value,  $D$  is the Earth–Sun distance in astronomical units (AU) at the time of observation, and  $E_0$  is the band-weighted solar irradiance at TOA, for average Earth–Sun separation ( $D = 1$ ). Ozone and out-of-band corrections are applied (Kahn et al. 2001b). Ozone amounts are given in Table 1, and the corrected  $\rho_{\text{MISR}}(\lambda, \mu)$  patch values are used in subsequent analysis. Figure 1, showing MISR true-color nadir or near-nadir views of each event, illustrates the relationships between patch locations and island AERONET sites. All are within 28 km of the AERONET site, and about 30% are within 10 km. Having data from multiple patches allows us to assess scene variability, which is important because we must compare nearly instantaneous MISR data averaged over 3.3 km with point data from nearby AERONET sites, sampled over 1–2-h periods.

Figure 2 illustrates MISR TOA equivalent reflectances for seven patches covering two representative events, as functions of MISR camera. Reflectance increases away from the nadir in both angular directions, as the line-of-sight path through the atmosphere increases. Equivalent reflectances are generally below 0.1 except for the steepest views in the blue band and are about 0.01 for the nadir view in the near-infrared band.

### b. AERONET data processing

The AERONET is a federation of autonomous Cimel sun- and sky-scanning photometers connected via satellite to a data analysis facility at the NASA Goddard Space Flight Center (Holben et al. 1998; <http://aeronet.gsfc.nasa.gov>). Standard processing automatically generates AOT in bands centered at about 340, 380, 440, 500, 675, 870, and 1020 nm, along with column water vapor, every 15 min under cloud-free, daylight conditions, from direct solar observations. Table 1 summarizes the AERONET AOT for each event, interpolated linearly to the centroid of the MISR green channel (558 nm) using the two AERONET channels nearest in wavelength. The numbers reported are for the measurements closest in time to the MISR overpass; all are coincident to within 30 min, and most are within 5 min. AERONET AOT uncertainties given in Table 1 represent measurement standard deviations over the averaging period.

TABLE 1. MISR-AERONET island site coincident observations.

Site	Latitude (°)	Longitude (°)	Date	MISR overpass time (UTC)	Terra orbit block	MISR path/ block	Sun zenith angle (°)	MISR cameras in sun glint <sup>a</sup>	Ozone column <sup>b</sup> (Dobson)	Wind speed <sup>b</sup> (m s <sup>-1</sup> )	Surface pressure (mb)	Airmass type	Aeronet AOT <sup>c</sup> (558 nm)	Aeronet SSA <sup>c</sup> (558 nm)	Aeronet scan time (UTC)
Bermuda	32.370	-64.696	19 Jun 2002	1511:30	13314	006/065	17.4	(Bf), Af, An, Aa	293	4.1 ± 0.7	1028	Maritime, dust possible	0.119 ± 0.006	0.90	2136
Bermuda	32.370	-64.696	21 Jul 2002	1511:47	13780	006/065	20.1	(Bf), Af, An, Aa	315	3.9 ± 0.7	1024	Maritime, pollution	0.288 ± 0.017	0.93	2219
Bermuda	32.370	-64.696	29 Aug 2002	1517:37	14348	007/064	27.1	(Cf), Bf, Af, An, (Aa)	303	3.6 ± 1.0	1020	Clean maritime	0.077 ± 0.006	0.99	2345
Bermuda	32.370	-64.696	14 Sep 2002	1517:38	14581	007/064	32.1	Cf, Bf, Af, An	292	5.8 ± 0.9	1025	Pollution possible	0.071 ± 0.01	0.98	2331
Lanai	20.735	-156.922	15 Mar 2000	2122:52	1289	064/074	28.2	Bf, Af, An	276	3.9 ± 0.8	1021.6	Maritime, pollution	0.044 ± 0.003	0.99	2345
Lanai	20.735	-156.922	10 Feb 2002	2107:15	11439	063/074	41.8	Bf, Af	255	1.6 ± 0.7	1018.6	Maritime, dust possible	0.12 ± 0.003	0.98	2331
Lanai	20.735	-156.922	17 Feb 2002	2113:22	11541	064/074	39	Cf, Bf, Af, An	245	1.6 ± 0.5	1018.5	Clean maritime	0.11 ± 0.005	0.95	2248
Lanai	20.735	-156.922	9 Jun 2002	2113:23	13172	064/074	17.1	Af, An, Aa, Ba	283	3.2 ± 0.3	1015.9	Clean maritime	0.107 ± 0.003	0.91	2136
Midway_Island	28.200	-177.367	9 Feb 2001	2242:06	6110	077/068	47	(Cf), Bf, (Af)	246	1.8 ± 1.0	1014.1	Clean maritime	0.062 ± 0.004	0.92	2204
Midway_Island	28.200	-177.367	7 Oct 2001	2232:04	9605	077/068	37	(Cf), Bf, Af	265	2.4	1018	Clean maritime	0.031 ± 0.001	0.97	2316
Midway_Island	28.200	-177.367	17 Dec 2001	2239:14	10639	078/068	54.1	Df, Cf, Bf, Af	242	5.85 ± 1.5	1022	Maritime, dust possible	0.046 ± 0.001	0.99	2345
San_Nicolas	33.250	-119.483	23 May 2002	1847:56	12923	041/064	19.4	(Bf), Af, An, Aa	336	2.2 ± 0.5	1012.9	Maritime, dust possible	0.112 ± 0.002	0.91	2150
San_Nicolas	33.250	-119.483	21 Apr 2002	1847:44	12457	041/064	26.4	Af, An, Aa	305	3.2 ± 0.7	1017.2	Dust possible	0.152 ± 0.002	0.96	2302
Rottmest_Island	-32.000	115.283	15 Jan 2002	0237:38	11049	114/116	26.9	Af, An, Aa, Ba	283	1.55 ± 0.5	1009.6	Clean maritime	0.103 ± 0.008	0.96	2302
Dry_Tortugas	24.600	-82.783	22 Apr 2002	1615:35	12470	016/071	21.6	Af, An, Aa	286	3.9 ± 0.5	1018.2	Continental	0.098 ± 0.005	0.93	2219

<sup>a</sup> An = nadir; Af, Aa=26.1° fore and aft; Bf, Ba=45.6° fore and aft; Cf, Ca= 60.0° fore and aft; Df, Da= 70.5° fore and aft. The An entries in parentheses have sun-glint angles of 38° and 39°, just below the 40° threshold, but appear to be unaffected by sun glint, so they are included in MISR-MODIS intercomparisons.

<sup>b</sup> Ozone column abundance is from the TOMS database ([http://toms.gsfc.nasa.gov/teacher/ozone\\_overhead.html](http://toms.gsfc.nasa.gov/teacher/ozone_overhead.html)); near-surface wind speeds and surface pressure are from the Weather Underground (<http://www.wunderground.com/history/station/78016/2002/8/29/DailyHistory.html>) for the appropriate station and date, except Lanai wind speed, which was obtained from the Western Regional Climate Center (<http://www.wrcc.dri.edu/cgi-bin/rawMAIN.pl?hiHKLL>).

<sup>c</sup> AOT, SSA, and  $n_i$  are interpolated linearly between the nearest AERONET channels, usually 501 nm and 675 or 676 nm. The numbers reported are the closest in time to the MISR overflight that are available. Uncertainties given for AOT are standard deviations of all available AERONET AOT measurements for ±1 h. Only green-band SSA is given here, but these are clean maritime particles, and SSA varies less than 0.01 over the wavelength range of interest, in almost all cases.

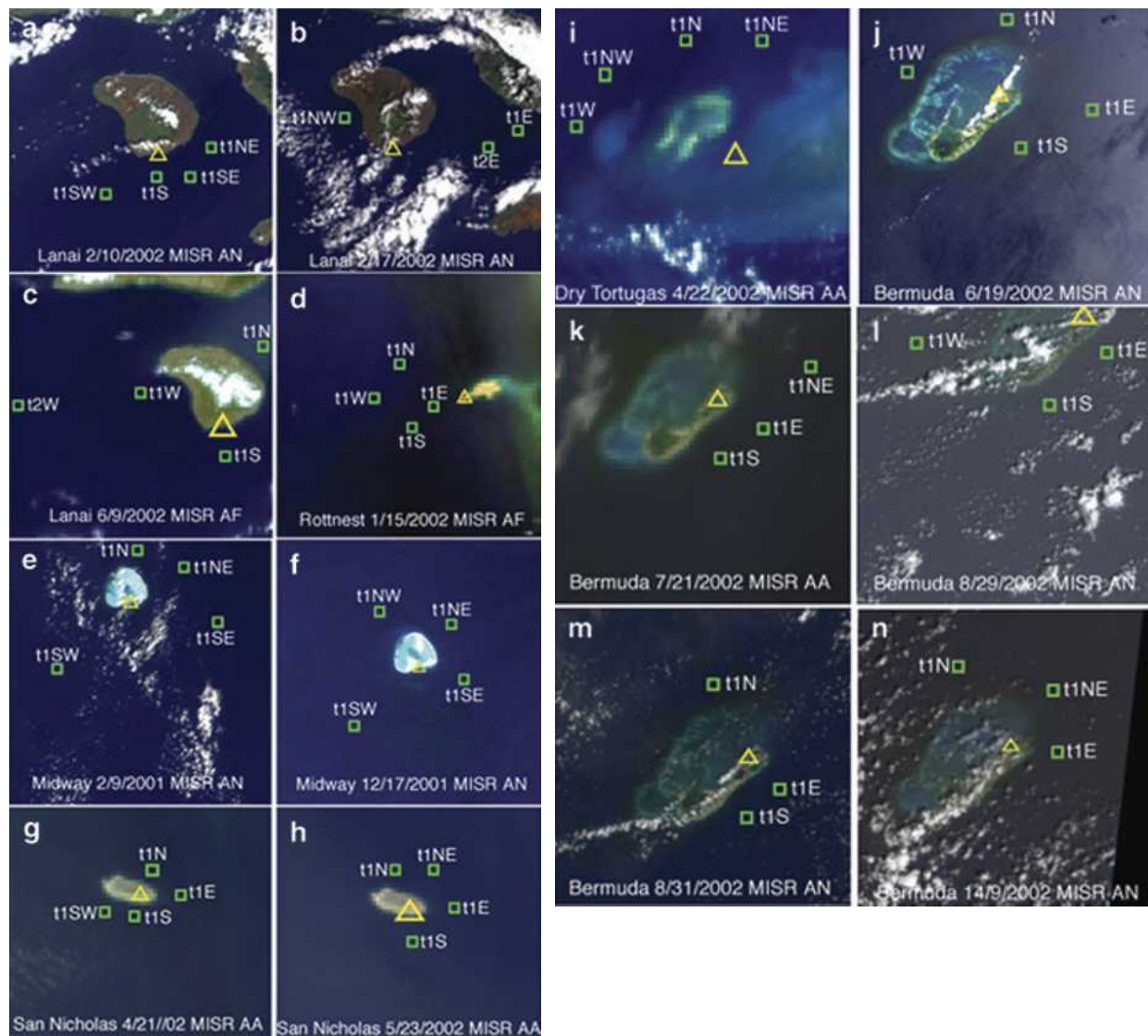


FIG. 1. MISR true-color nadir (AN) or near-nadir (AF, AA) views for the cases used in this study. The AERONET site in each image is indicated by a triangle, and the locations of the MISR analysis patches are marked with labeled green boxes. (a) Lanai on 10 Feb 2002; (b) Lanai on 17 Feb 2002; (c) Lanai on 9 Jun 2002; (d) Rottneast on 15 Jan 2002; (e) Midway on 2 Feb 2001; (f) Midway on 17 Dec 2001; (g) San Nicholas on 21 Apr 2002; (h) San Nicholas on 23 May 2002; (i) Dry Tortugas on 22 Apr 2002; (j) Bermuda on 19 Jun 2002; (k) Bermuda on 29 Aug 2002; (l) Bermuda on 19 Jun 2002; (m) Bermuda on 31 Aug 2002; and (n) Bermuda on 14 Sep 2002.

The AERONET sun photometers are also programmed to perform sky scans in the principal plane and across the almucantar at 440, 670, 870, and 1020 nm about once per hour, from which aerosol size distribution is derived (Dubovik and King 2000; Dubovik et al. 2002). This process is independent of the 15-min AOT retrievals, which are obtained from direct transmission, calibrated using the Langley method. A combination of direct-sun and sky-scan data is used to retrieve spectral indices of refraction. We selected the best-quality aerosol property retrievals close in time to the MISR overpasses. Observation times are less closely matched than

for the AOT data—usually under 30 min, though for several events, such as Bermuda on 19 June 2002, the gap is 2–3 h, and for Dry Tortugas on 22 April 2002 and Lanai on 9 June 2002, good-quality retrievals were obtained only about 4 h ahead of MISR imaging (Table 1). Retrieved size is reported as relative volume-weighted amount at 22 values of particle radius, spread logarithmically between 0.05 and 15  $\mu\text{m}$ . Size distributions are also provided by AERONET standard processing as parameter fits to lognormal functions, but we favor the histogram data here, since they offer a consistent fit to the observed radiation field.

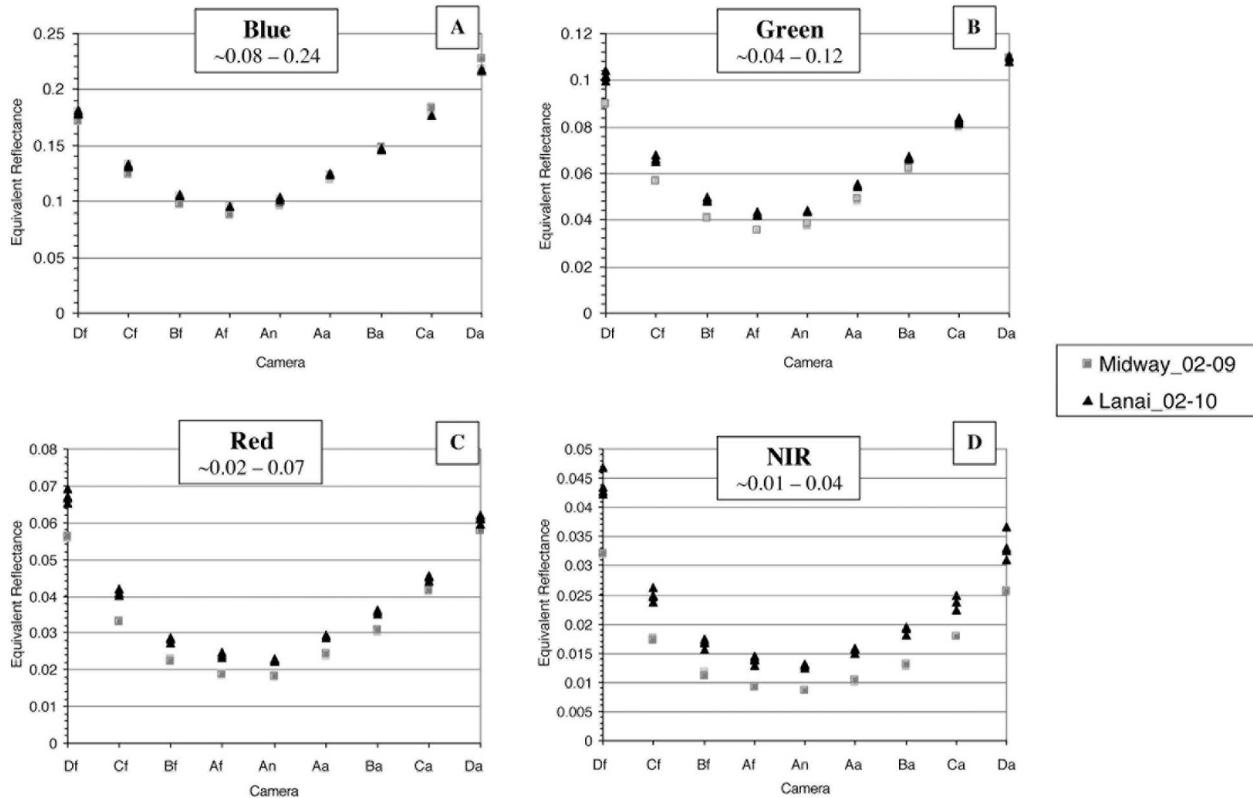


FIG. 2. Observed TOA reflectances for three Midway-event patches on 9 Feb 2001 and for four Lanai patches on 10 Feb 2002. The horizontal axes show MISR cameras arranged by viewing sequence, from the 70° and 60° forward views (cameras Df and Cf, respectively) through nadir (camera An), to the 60° and 70° aft-viewing cameras (Ca and Da). The four plots show the MISR (a) blue, (b) green, (c) red, and (d) near-infrared spectral bands. Note that the vertical scale varies from plot to plot.

We work with level 1.5, or when available, level 2 AERONET products. For level 1.5, basic quality control has been performed, including cloud screening that relies on AOT variability among three direct-sun observations taken 1 min apart, on each 15-min measurement center (Smirnov et al. 2000). The level 2 products have been further refined, using sun photometer calibration data taken after the measurements of interest, in addition to the precalibration data required for level 1.5. Direct-sun AOT retrievals are generally believed to be accurate to about 0.01 or 0.02 for midvisible wavelengths. The highest-quality particle property retrievals are obtained for solar zenith angles greater than 45° and for AOT (at 440 nm) greater than about 0.4 (Dubovik et al. 2000). Since low AOT values and small solar zenith angles are of interest in the present study, we selected specific sky-scan instances for which the algorithm performed well and retrieved reasonable particle size distributions, based on the experience of the AERONET team (Fig. 3a).

We expect the retrieved index of refraction to be less certain than the size distribution at low AOT. The sun photometer does not directly observe the full angular range; an assumption must be made to assess the missing parts of the scattering phase function, and particle

absorption, which depends on an integral over all scattering angles, is sensitive to this assumption. In addition, the index-of-refraction retrieval relies on both sky scans (for scattering information) and direct-sun AOT retrievals (for extinction information), whereas size distribution is determined from sky scans alone. Small AOT variations in the time between sky scans and direct-sun observations can affect the resulting index of refraction, and sky scans are cloud screened based on radiance symmetry across the almucantar, which may be more sensitive to very thin cloud than the variability criterion used for AOT retrievals. If the AOT is as little as 0.01 higher during the AOT measurement than the sky-scan observation, the retrieved imaginary index of refraction will be erroneously high, which can artificially lower the derived particle SSA by ~10%. Instrument sun-channel absolute calibration, nominally 0.01 in AOT units, may also be a factor; at 0.05 AOT, the formal calibration error is 20%, though AOT variability for measurements covering several hours can be as low as 0.001 for the events of interest (Table 1). Under the relatively clean maritime aerosol air masses selected for this study, we expect midvisible SSA to be at least 0.90 (e.g., Smirnov et al. 2003; Shettle and Fenn 1979). So,

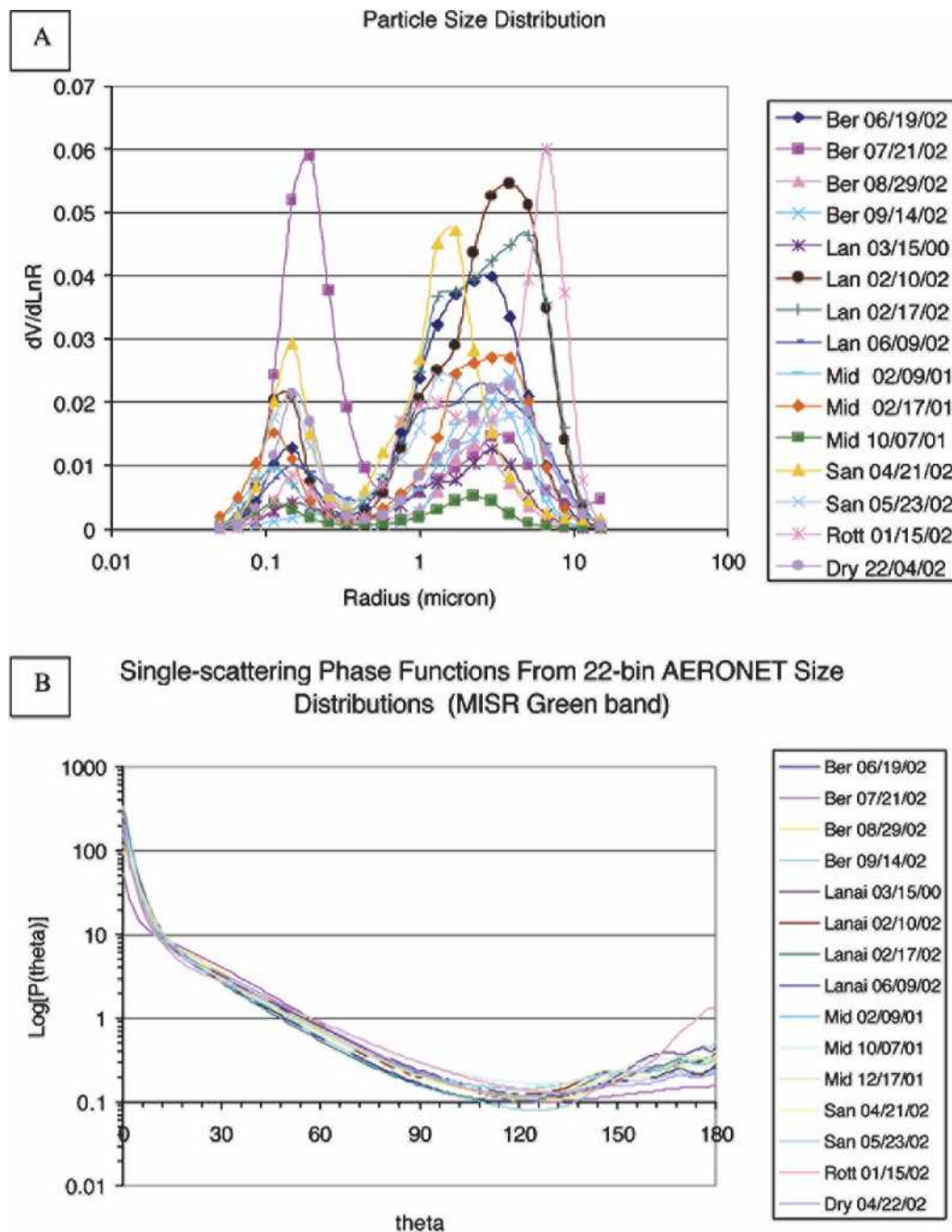


FIG. 3. (a) Volume-weighted particle size distributions retrieved by AERONET for 15 MISR–AERONET coincident cases. Each plot is roughly bimodal, defined by points in 22 size bins that are connected with curves for clarity. (b) Particle single scattering phase functions derived using a Mie code, for the 15 AERONET-retrieved particle size distributions shown in Fig. 3a. For this figure, “theta” is the scattering angle in degrees.

in addition to considering the standard AERONET quality factors for each event, we eliminated those events having retrieved indices of refraction that produced SSA below 0.90, and treated all SSA values below 0.98 as uncertain to within  $\pm 0.03$ .

### 3. Reflectance modeling and confidence levels

Since we selected cases for which clean maritime aerosols are expected, we assume spherical particles and simulate extinction cross sections, SSA, and single

scattering phase functions in the four MISR bands with a Mie scattering algorithm, using the AERONET-derived size distributions and indices of refraction for each event. MISR green-band single scattering phase functions are shown in Fig. 3b, and SSA is given in Table 1, for each case. The resulting spectral extinction ratios agree with the corresponding AERONET direct-sun retrievals to better than the 0.01 to 0.02 uncertainty in the individual AOT measurements themselves.

We then calculate the TOA equivalent reflectance for all 36 MISR channels with the MISR standard radiative transfer code (MISR-RT; Martonchik et al. 1998). Given sun- and camera-viewing geometry, surface pressure, aerosol optical properties and amount, and near-surface wind speed, the model calculates TOA reflectance  $\rho_{\text{model}}$

$$\rho_{\text{model}}(\mu, \mu_0, \phi; \lambda) = \rho_{\text{atm}} + \rho_{\text{dir}}[\rho_{0(\text{glt}+\text{wcp})}(\text{wnd}), A_0(\lambda)] \\ + \rho_{\text{dif}}[\rho_{0(\text{glt}+\text{wcp})}(\text{wnd}), A_0(\lambda)], \quad (2)$$

where  $\mu_0$  is the cosine of the sun zenith angle,  $\phi$  is the azimuth angle between the sun and view directions, and  $\text{wnd}$  is the wind speed;  $\rho_{\text{atm}}$  is the atmospheric path reflectance, characterizing light scattered by the atmosphere that does not reach the surface, and  $\rho_{\text{dir}}$  and  $\rho_{\text{dif}}$  are the direct and diffuse transmittance of light through the atmosphere, respectively. The second and third terms on the right-hand side are the direct and diffuse surface contributions, respectively. The term  $\rho_{0(\text{glt}+\text{wcp})}$  is the reflectance emanating from the ocean surface due to Fresnel reflection plus wind-speed-dependent glint and whitecaps, calculated using standard models (Martonchik et al. 1998; Kahn et al. 2001b).

The water-leaving reflectance,  $A_0(\lambda)$ , arises from light scattered by silt, phytoplankton, and pollutants in surface waters and is distinct from the Fresnel reflection plus wind-dependent glint and whitecap contributions. For dark water, containing little silt or biological material,  $A_0$  is small in the midvisible and diminishes with increasing wavelength. We assume  $A_0$  to be wavelength dependent but independent of view angle (Lambertian); for the conditions of interest,  $A_0$  should vary no more than 4%, due to non-Lambertian effects, except possibly in the blue channel, and then only for very low chlorophyll concentrations (Yang and Gordon 1997).

We adopt nominal  $A_0$  values of 0.03, 0.007, 0.002, and 0.0007 in the MISR blue, green, red, and near-infrared bands, respectively, for ocean away from continents (e.g., Morel and Maritorena 2001). Water-leaving reflectance is measured on a continuing basis by the Marine Optical Buoy (MOBY) near Lanai, Hawaii, a clean ocean site (Clark et al. 1997). There is coincident data for the 10 February 2002 MISR–AERONET event; for this and other Lanai events we use the  $A_0$  values measured on that day, 0.022, 0.004, 0.0005 for the blue, green, and red bands, respectively. For the near-

infrared band,  $A_0$  was too small to measure, well below the nominal value of 0.0007.

To complete the model inputs, we calculate view angle geometry specific to each patch. We adopt locally measured surface pressure in each case for calculating atmospheric Rayleigh scattering (Table 1) and assume the aerosols to be confined to the lowest 10 km of the atmosphere, with a number concentration having a 2-km-scale height. Away from sources (including sea salt, because these are low-wind cases), aerosols typically have vertical distributions as assumed, and since clean maritime aerosols have high SSA, the TOA reflectance is not very sensitive to assumed aerosol vertical distribution.

The model atmospheric path reflectance, direct surface reflectance, and diffuse surface reflectance contributions at TOA are shown in Fig. 4 for a low-AOT event. The atmospheric contribution dominates in all cases, and the Rayleigh optical depth exceeds the aerosol optical depth in the blue and green bands.

We expect TOA radiance sensitivity to model parameters to vary with view angle and wavelength. As shown in Fig. 4, the surface fractional contribution is largest for the nadir and near-nadir views, which are therefore most sensitive to the surface model. Radiance is highest in the oblique views, since the atmospheric path is greatest, and for the shorter wavelengths, because of larger Rayleigh, aerosol, and surface contributions. These channels should be most sensitive to the atmospheric model. Also, as AOT increases for these low-light-level scenes, the signal-to-noise ratio increases, and sensitivity to the surface model is reduced.

A detailed look at model sensitivity to key inputs is presented next.

#### a. Aerosol optical thickness sensitivity

Since the MISR patches are over dark water up to 28 km away from the AERONET sites, assessing AOT variability is more important for radiance comparisons than obtaining exact temporal coincidence. In Table 1, AOT variability is given as the standard deviation of all available AERONET AOT measurements within  $\pm 1$  h of the MISR overpass. In 12 cases, the standard deviations are 0.006 or less. For the most variable events, Bermuda on 14 September and 21 July, AOT changed no more than 15% in available data during the 2-h window. Except for these cases, AERONET AOT remained within a few percent or less of its value at MISR overpass time.

We evaluated the modeled reflectance uncertainty due to AOT variations by simulating with the forward radiative transfer model the TOA reflectance in all 36 MISR channels, for the event-specific AERONET AOT variation and other parameters fixed at the nominal values reported in Table 1. Maximum simulated reflectance variations for each MISR band, assessed over all non-sun-glint-contaminated views, are given in the first data block of Table 2. TOA reflectance varia-

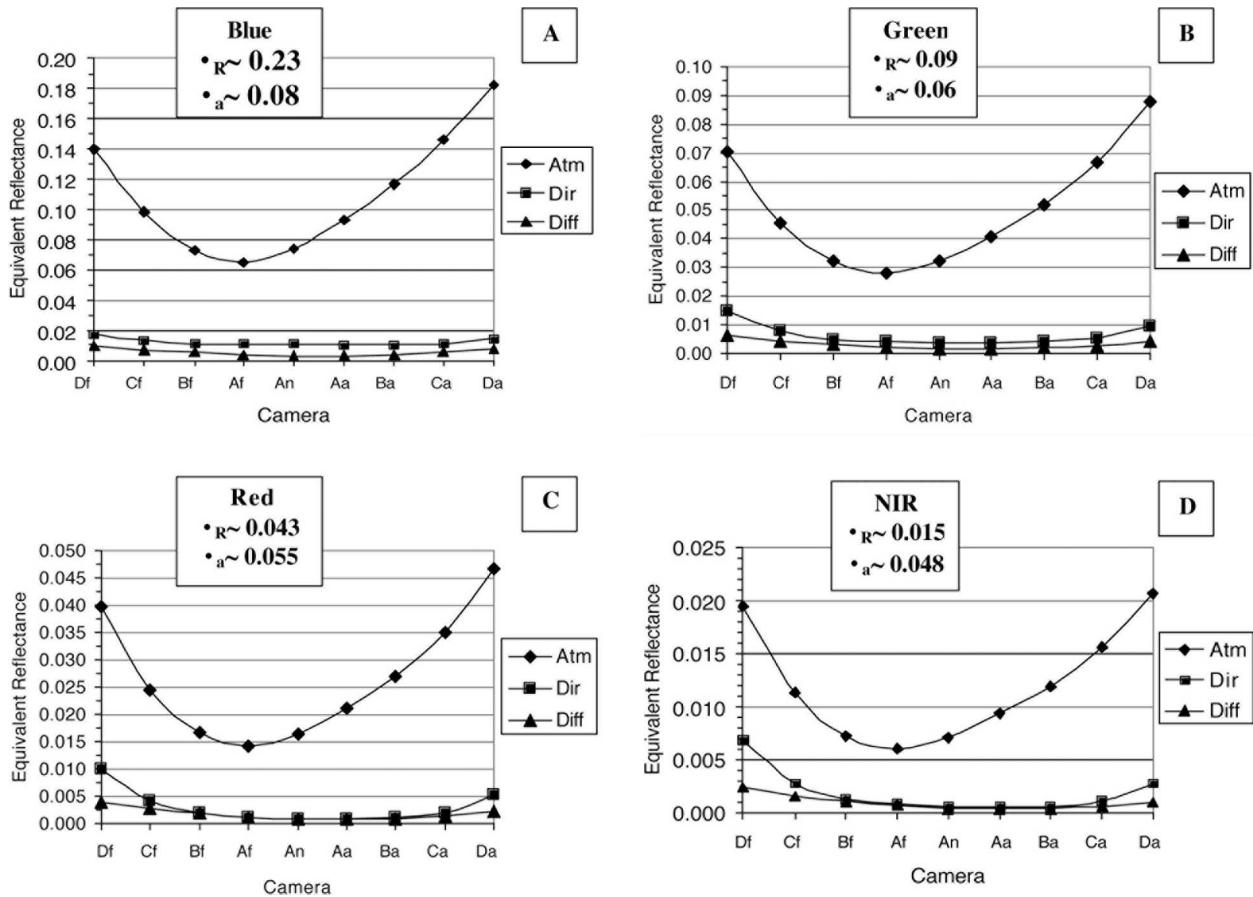


FIG. 4. Modeled atmospheric path reflectance, direct surface reflectance, and diffuse surface reflectance, as functions of MISR camera, all evaluated at TOA, for the Midway event on 9 Feb 2001, patch tln. The Rayleigh and aerosol optical depths ( $\tau_R$  and  $\tau_a$ ) are also given. The four plots show the MISR (a) blue, (b) green, (c) red, and (d) near-infrared spectral bands.

tions are greatest for the near-infrared channel and diminish systematically with decreasing wavelength due to the moderating effect of Rayleigh scattering by atmospheric gas, a significant contributor at low AOT. Typical Rayleigh optical depths are only about 0.015 in the near-infrared, but reach 0.23 in the blue (Fig. 4). The larger-AOT-variability events mentioned above stand out as the only ones having maximum uncertainty greater than 2% in the red band. Typically, the relative errors in TOA reflectance due to AERONET-derived AOT uncertainty are about 0.3%, 0.5%, 0.7%, and 1% in the blue, green, red, and near-infrared bands, respectively.

#### b. Aerosol single scattering albedo sensitivity

We treat SSA as uncertain in the MISR green band to within  $\pm 0.03$  of the nominal AERONET value (Table 1), based on reported sensitivity estimates (Dubovik et al. 2000), and scale the assumed perturbations in the other bands proportionately. (Since these are clean maritime particles, SSA itself varies little with wavelength.) We calculate optical properties for the

perturbed particles with Mie scattering, then assess the impact of these changes on TOA reflectance using the forward radiative transfer model, as we did for AOT. Maximum uncertainty obtained for each MISR band, assessed over all non-sun-glint-contaminated views, is given in the second data block of Table 2. SSA sensitivity varies systematically with wavelength as does AOT and is greatest for the near-infrared because of the lack of compensating radiance from other sources. It is also larger at shorter wavelengths for events having larger AOT, such as Bermuda on 21 July. Maximum TOA reflectance uncertainties based on these SSA perturbations are generally less than 1.5% in the blue and green, 2.5% in the red, and 3.5% in the near-infrared.

#### c. Wind speed sensitivity

Wind speeds given in Table 1 for each event were measured near the AERONET stations, but must be considered uncertain when applied to patches some distance away. We use a standard approach to modeling the effect of wind speed on ocean surface whitecap reflectivity (Koepke 1984; Monahan and Muircheartaigh

TABLE 2. Model TOA reflectance uncertainty estimates (%) for MISR-AERONET coincident observations for the blue (B), green (G), red (R), and near-infrared (NIR) bands. For each site and band, maximum uncertainties are evaluated from among all view angles not in sun glint.

Site	Date	Max uncertainty from AOT (%)			Max uncertainty from SSA (%)			Max uncertainty from wind speed (%)			Max total uncertainty (%)			Avg total uncertainty (%)							
		B	G	R	B	G	R	B	G	R	B	G	R	B	G	R					
Bermuda	29 Aug 2002	1.07	1.91	2.73	3.83	1.22	1.58	1.94	3.21	0.41	0.90	2.06	5.16	1.60	2.50	3.48	6.67	1.23	1.87	2.69	4.48
Bermuda	14 Sep 2002	0.83	1.59	2.84	5.38	1.20	1.55	2.16	3.40	0.26	0.90	1.97	4.32	1.22	2.18	4.08	7.70	1.06	1.68	2.86	5.39
Bermuda	19 Jun 2002	0.31	0.82	1.50	2.76	1.21	1.67	2.17	3.40	0.22	0.53	1.12	2.25	1.26	1.86	2.72	4.69	1.17	1.75	2.55	4.30
Bermuda	21 Jul 2002	1.34	2.44	3.38	4.30	3.51	4.02	4.21	4.30	0.13	0.27	0.61	1.45	3.68	4.55	5.23	5.94	3.43	4.22	4.92	5.72
Lanai	10 Feb 2002	0.42	0.84	1.27	1.84	1.68	2.20	3.14	4.69	0.29	0.36	0.35	0.47	1.75	2.33	3.27	4.93	1.49	2.06	2.78	3.86
Lanai	17 Feb 2002	0.53	1.27	2.12	3.24	1.46	2.20	3.17	5.23	0.21	0.24	0.25	0.42	1.55	2.52	3.63	5.78	1.33	2.11	3.08	4.90
Lanai	9 Jun 2002	0.26	0.57	0.93	1.49	1.20	1.76	2.47	3.77	0.11	0.30	0.65	1.45	1.22	1.85	2.64	4.06	1.07	1.56	2.26	3.71
San Nicolas	23 May 2002	0.16	0.37	0.62	1.00	1.28	1.73	2.31	3.50	0.19	0.25	0.26	0.35	1.30	1.79	2.40	3.63	1.16	1.57	2.14	3.38
San Nicolas	21 Apr 2002	0.20	0.42	0.64	0.94	1.99	2.52	3.43	5.82	0.26	0.46	0.94	1.76	2.01	2.58	3.47	5.89	1.75	2.34	3.07	4.52
Midway Island	17 Dec 2001	0.09	0.20	0.38	0.62	0.61	0.95	1.39	2.09	0.32	0.50	1.08	2.64	0.69	1.03	1.74	3.35	0.57	0.97	1.60	2.75
Midway Island	9 Feb 2001	0.69	1.47	2.32	3.62	0.88	1.34	1.95	3.53	0.40	0.43	0.66	1.09	1.17	2.04	3.05	4.83	0.83	1.42	2.26	4.01
Dry Tortugas	22 Apr 2002	0.47	1.02	1.71	2.81	1.17	1.51	1.82	2.50	0.17	0.25	0.47	1.03	1.24	1.82	2.51	3.75	1.12	1.62	2.26	3.51
Rottnest Island	15 Jan 2002	1.22	2.43	3.68	5.38	1.50	2.10	2.76	3.48	0.21	0.26	0.24	0.31	1.88	3.18	4.53	6.33	1.60	2.49	3.68	5.57

1980). The resulting whitecap model reflectance is uncertain to 20% or 30%, which becomes significant at high wind speeds. So for this study, we include only events having wind speeds well below  $7.5 \text{ m s}^{-1}$  (Table 1), the value above which whitecap reflectivity is large enough to degrade overall confidence in the model results. Note that reflectance sensitivity to wind speed depends on AOT and view angle, as well as on the wind speed itself.

The effect of wind speed uncertainty has higher spectral dependence than that of AOT and SSA uncertainty; it is also greatest for the near-infrared channel and diminishes dramatically with decreasing wavelength. Whitecap reflectance is modeled as spectrally neutral across the visible spectrum up to about 900 nm (Koepke 1984). But the calm surface, atmospheric gas, and aerosol all contribute less to the TOA reflectance in the near-infrared than at shorter wavelengths. So, for a camera not in sun glint, a spectrally neutral whitecap contribution has an even larger impact on spectral dependence than a perturbation to aerosol properties. Specifically, the change in TOA equivalent reflectance for the highest wind speed event, Midway, on 17 December, is 2.6% in the near-infrared, though the magnitude of the reflectance itself is just 0.01 to 0.03.

For even lower wind speed events, the sensitivity is further reduced. For example, by increasing the wind speed from  $0.8$  to  $2.8 \text{ m s}^{-1}$  for the 9 February Midway event, bracketing the  $1.8 \text{ m s}^{-1}$  value observed in the area, the reflectance increased by 0.4% in the blue and green, 0.7% in the red, and 1.1% in the near-infrared.

In some cases, the limited width of the sun-glint pattern provides an independent test that the wind speed was below the threshold for producing significant whitecap contributions. For Bermuda on 21 July, the MISR Af, An, and Aa cameras, having sun-glint angles of  $25^\circ$ ,  $17^\circ$ , and  $35^\circ$ , respectively, all observed glint (Table 1). Had the wind speed been much greater than about  $7 \text{ m s}^{-1}$ , the glint pattern would have entered the Bf camera, at a sun-glint angle of  $42^\circ$ . Had that occurred, the pixel-to-pixel variability over a  $3 \times 3$  patch would have been at least 3 times higher for that camera than for the non-sun-glint-contaminated cameras (Kahn et al. 2001b), which it was not.

*d. Formal confidence-level calculations from AOT, SSA, and wind uncertainties*

We assume the uncertainties in total column optical depth, particle single scattering albedo, and near-surface wind speed are independent, so the confidence level for each simulated measurement is the square root of the sum of squares of the three uncertainty estimates (Table 2). The maximum total uncertainty in each MISR band, for all views not in sun glint, is reported in the fourth data block of Table 2, and the average total uncertainty is given in the final data block.

These confidence-level magnitudes are not measurement errors. They are indications of the degree to

which the comparison models for these specially selected events are constrained by observations. Since we are interested in the best-constrained cases for this study, we eliminated the events having confidence levels poorer than 4%, except in the near-infrared band, where we set the cutoff at 6%. In most cases, the maximum total uncertainty is below 3% in all bands except the near-infrared. Average cumulative model uncertainty due to AOT variability, wind speed variability, and SSA uncertainty is typically  $\sim 1\%$ ,  $1\%–2\%$ ,  $1.5\%–3\%$ , and  $2.5\%–4\%$  in the blue, green, red, and near-infrared channels, respectively, for the events chosen.

*e. Aerosol size distribution, spectral assumption, and numerical algorithm sensitivity*

We have no formal variability ranges over which to assess aerosol size distribution confidence levels. But the AERONET standard product reports size distributions as bimodal, volume-weighted lognormal distributions fitted to the retrieved 22-bin size spectrum, so we

arbitrarily perturb the effective radius and distribution width for each mode by  $\pm 10\%$ . We also perturb the ratio of medium- to coarse-mode amount by  $\pm 10\%$  and renormalize the distribution in each case (Fig. 5). Percent variation increases with wavelength as the stabilizing influence of Rayleigh scattering is reduced, and is not more than 1% in the MISR blue band, 2% in the green, or 3.5% in the red. The near-infrared channel has very low signal for low-light-level events, which contributes to higher percent sensitivity. Percent variation generally increases away from nadir (the An camera in Fig. 5), as the aerosol component of the TOA reflectance increases, and is asymmetric about the nadir view because of scattering angle differences (Table 3). We exclude size distribution sensitivity from the formal confidence-level calculations because we have no event-specific measure of variability, as we do for AOT and wind speed, and since the actual size distribution uncertainty is probably lower than that for SSA, relative to their nominal values, as discussed in section 2b.

We assessed the consequences of using particle prop-

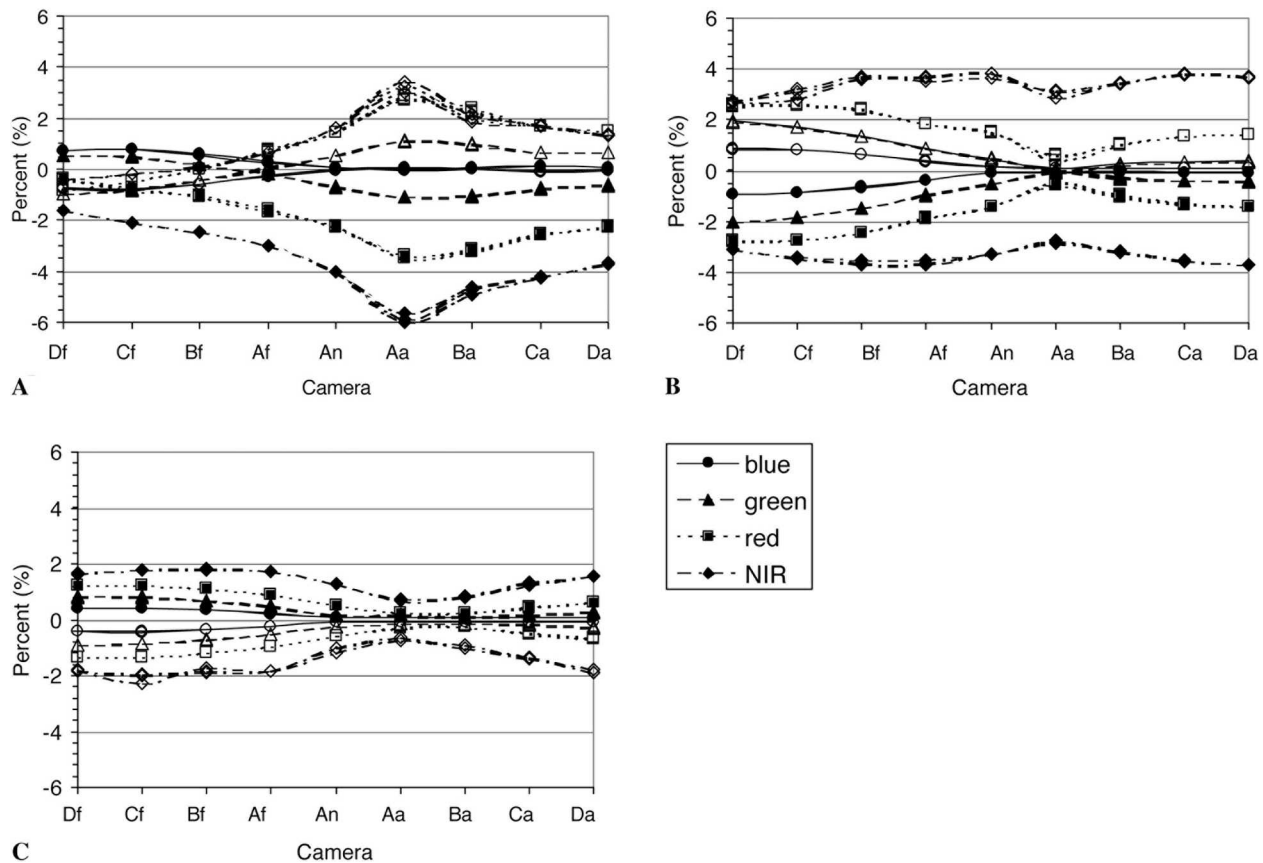


FIG. 5. Particle size distribution sensitivity study. Percent change in TOA reflectance is shown for all 36 MISR channels, produced by  $\pm 10\%$  perturbation from nominal AERONET values, in each of (a) medium-mode effective radius, (b) medium-mode distribution width, and (c) ratio of medium-to-large modes, for three patches from the Lanai event on 10 Feb 2002. Smaller changes are produced by these perturbations for lower-AOT events, such as Midway on 9 Feb 2001. Open symbols are for positive perturbations, solid symbols for negative ones. In each case, perturbed particle properties were generated using a Mie scattering code.

erties evaluated only at the MISR band effective wavelengths. Using a Simpson's Rule integration over the spectral band, we found the differences to be negligible relative to other uncertainties in these calculations. We also tested the MISR-RT itself against the Coupled Ocean-Atmosphere Radiative Transfer (COART) model produced by Jin et al. (2002; <http://snowdog.larc.nasa.gov/jin/rtset.html>). To avoid introducing reflectance discrepancies of a percent or larger, view angles must be specified to better than  $0.5^\circ$  in each calculation, especially for the steeply viewing C and D cameras. Fortunately, MISR pointing accuracy is better than  $0.006^\circ$  for all cameras (Jovanovic et al. 2002). Also, the MISR-RT code includes a view-angle-dependent polarization correction for the gas component, derived from vector calculations, that amounts to as much as 4% in the blue band, less in the other bands. This term was eliminated from the MISR-RT results for the purpose of comparison with COART, since it is not included in the COART code but is retained for all other calculations in this paper.

Differences between the COART and MISR-RT models in each MISR channel, for atmospheric gas (Rayleigh) scattering only, and gas plus aerosol, are shown in Fig. 6. Since the reflectance magnitudes decrease with wavelength, the percent differences for

both gas alone and gas plus aerosol increase with wavelength. Differences between the MISR-RT and COART atmospheric terms amount to about 0.7% or less in the blue, about 2% for the red band, 2.5% for the green, and 3% for the near-infrared. These differences are traced to variations in the assumed vertical distribution of gas relative to aerosol in the two models, and for the green band, to gaseous absorption included in COART but not in MISR-RT. A large change in scattering angle between the Da and the other aft-viewing cameras (Table 3) seems to account for the decreased Da camera residuals.

The analysis presented in this section highlights the sensitivity of the multiangle technique to environmental factors, as well as the need for precision in many aspects of comparison model calculations. Estimated uncertainties are smallest for the shorter wavelengths, in part because of the stabilizing effect of well-constrained gas scattering and in part because of higher absolute reflectances. However, uncertainties in ocean surface reflectance contribute most to the blue and green channels, especially in the nadir and near-nadir views. For well-constrained events, we expect model reflectance relative accuracy to be 4% or better in all but the near-infrared channel. To develop confidence in low-light-level vicarious calibration results to a few

MISR-COART Comparison Without Polarization Correction

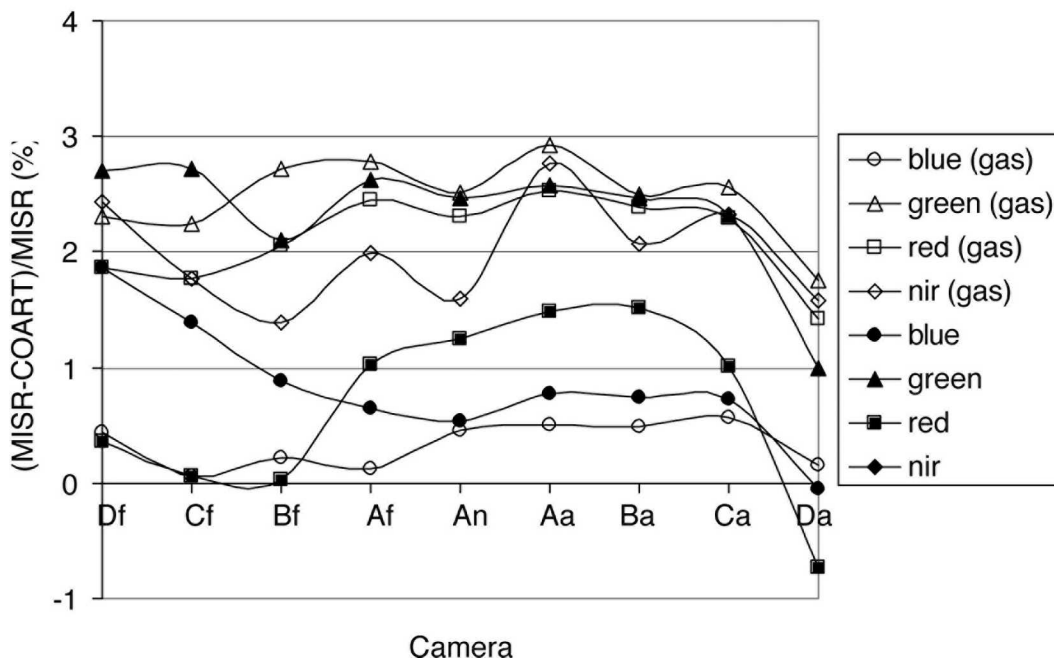


FIG. 6. Comparisons between the MISR-RT and COART radiative transfer code reflectances for the 9 Feb 2001 Midway event, giving atmospheric gas only and gas + aerosol results. The quantity plotted is  $(\text{MISR-RT} - \text{COADS}) / \text{MISR-RT} \times 100$ . The polarization adjustment in the MISR-RT code has been removed for the purposes of this comparison. Note that the magnitudes of percent differences are affected by lower absolute reflectances at longer wavelengths (Fig. 2).

TABLE 3. Scattering angles for each MISR camera, Lanai, and Midway cases, where An = nadir; Af, Aa=26.1° fore and aft; Bf, Ba = 45.6° fore and aft; Cf, Ca = 60.0° fore and aft; and Df, Da = 70.5° fore and aft.

Patch	Df	Cf	Bf	Af	An	Aa	Ba	Ca	Da
Lanai_02-10-02									
t1ne	83.0	92.3	105.4	122.8	144.0	156.3	150.9	141.0	132.6
t1s	83.3	92.7	105.9	123.4	144.9	157.6	151.8	141.5	133.0
t1se	83.3	92.7	105.9	123.4	144.9	157.6	151.8	141.5	133.0
t1sw	83.6	93.1	106.4	124.0	145.8	158.8	152.7	142.1	133.4
Midway_02-09-01									
t1n	76.1	85.7	99.3	117.3	140.4	158.9	159.0	149.7	141.2
t1ne	76.1	85.7	99.3	117.3	140.4	158.9	159.0	149.7	141.2
t1se	75.9	85.5	98.9	116.9	139.8	157.8	157.8	148.9	140.6
t1sw	76.7	86.5	100.2	118.4	141.7	160.9	160.7	150.7	141.8

percent, we must rely on patterns in band-to-band, camera-to-camera, and absolute reflectance differences that recur among several of the best cases.

#### 4. Equivalent reflectance comparisons

We obtain estimated TOA reflectance residuals for each patch, in all 36 MISR channels, by comparing the observed reflectance with that calculated from the model, constrained by AERONET and other inputs:

$$\rho_{\text{resid}}(\mu, \lambda; A_0) = \rho_{\text{MISR}}(\mu, \lambda) - \rho_{\text{model}}(\mu, \lambda; A_0). \quad (3)$$

MISR residuals are shown in Fig. 7, for 44 patches, covering 14 events at five island sites, expressed as the percent of  $\rho_{\text{MISR}}$  for each case. Points are color coded by site. There is considerable scatter in the data, but the residuals are almost all positive, and the camera-to-camera pattern is very similar, though displaced vertically, depending on the site. For example, the Bermuda and San Nicholas events fall at the high end of the distribution. No measurements of spectral water-leaving reflectance were available for these sites, but the assumed values of  $A_0$  may account for some of these differences. As shown in Fig. 8, an  $A_0$  value be-

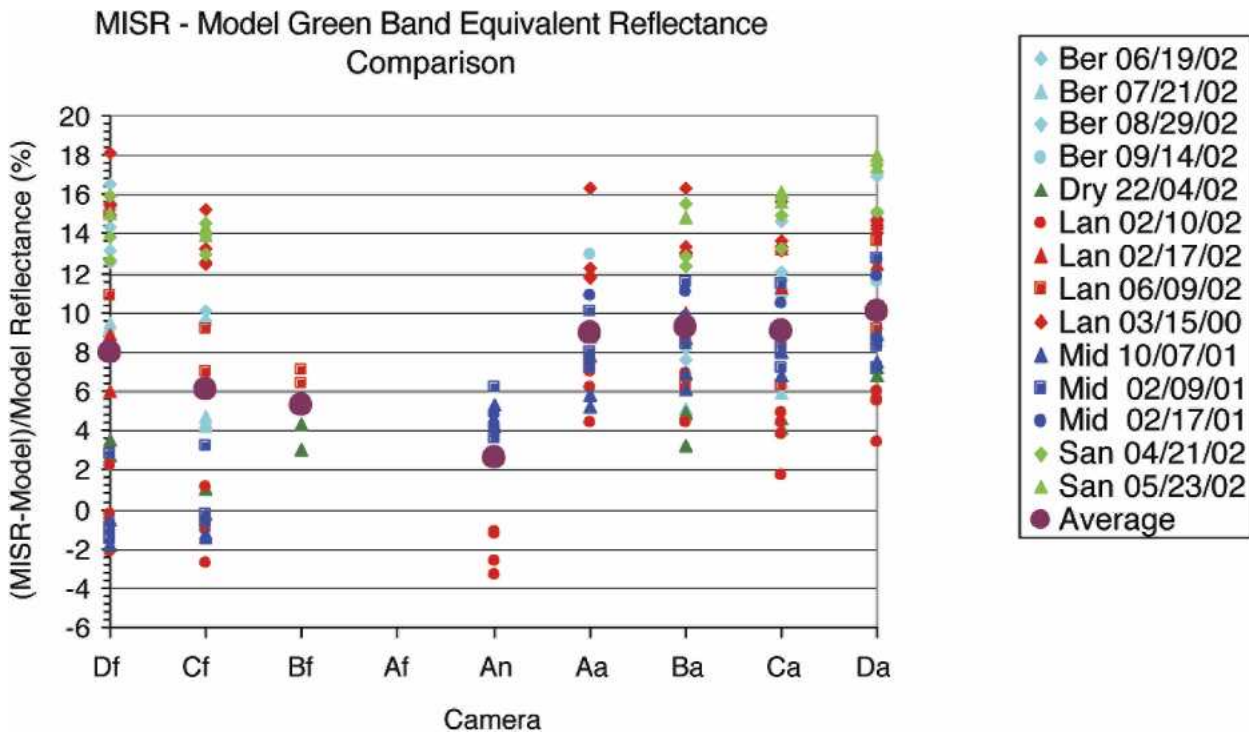


FIG. 7. MISR-model green-band residuals for 44 patches, covering 14 events at five island sites, expressed as a percent of  $\rho_{\text{MISR}}$  for each case, arranged by MISR camera. Sun-glint-contaminated views have been omitted. All events for a given site are assigned the same color, and all patches for a given event have the same symbol. The average of all points for each camera is indicated as a large purple dot. No values appear for the Af camera because this view is sun-glint contaminated in all available cases; there are fewer points for the Bf and An cameras for the same reason.

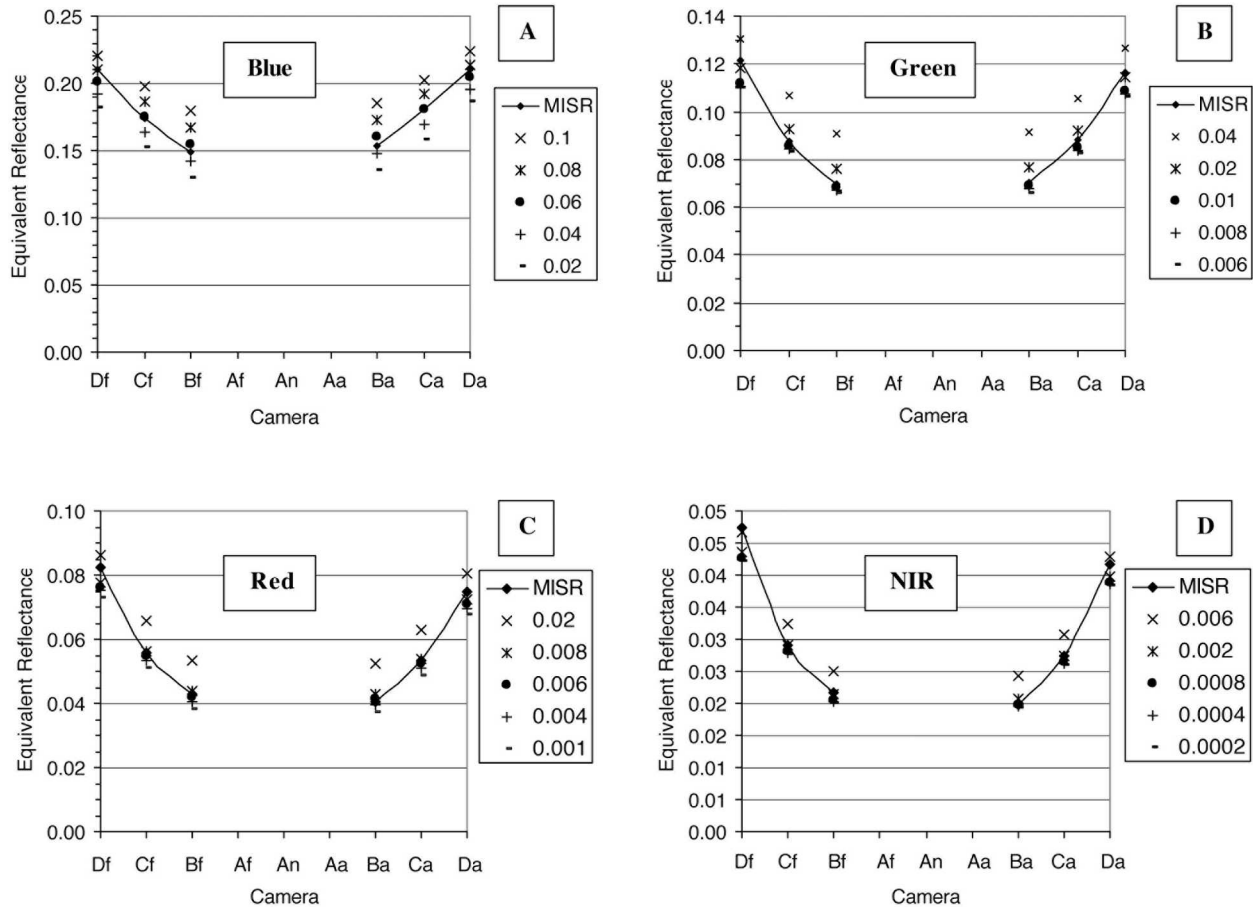


FIG. 8. MISR reflectances for the Bermuda event on 21 Jul 2002 with model results for varying water-leaving reflectance ( $A_0$ ) superposed. All cameras not in sun glint for this event are included. The four plots show the MISR (a) blue, (b) green, (c) red, and (d) near-infrared spectral bands. Note that the vertical scale varies from plot to plot.

tween the nominal 0.0007 and 0.001 in the near-infrared channel, and one between the nominal 0.002 and 0.008 in the red, produces model reflectances that bracket the MISR observations for the Bermuda event on 21 July 2002. Particularly in the steeply viewing Df and Da cameras, larger discrepancies appear for the blue channel, where reflectance agreement is reached when  $A_0$  is between 0.04 and 0.08, and the green, where values between 0.006 and 0.01 are needed. The atmospheric model is the likely cause; this is the highest AOT event in the dataset (Table 1), so sensitivity to aerosol optical properties is greater than for all other cases (Table 2). These observations indicate limitations in our ability to constrain the model calculation with available data and stress the importance of using the best-constrained events to quantify the vicarious calibration scale.

Midway and Lanai offer the cleanest island cases in Fig. 7. Midway on 9 February 2001 and Lanai on 10 February 2002 also have the advantage of being glint free in the nadir view (Table 1), so we can in addition compare reflectances with those obtained simultaneously by MODIS. Also, for the Lanai event, we have direct measurements of  $A_0$  from MOBY.

#### a. Band-to-band and absolute calibration tests: Nadir views

We compare in Fig. 9 equivalent reflectances from the MISR nadir view, the AERONET-constrained model, and eight spectrally nearby MODIS channels (four channels optimized for land observation and four aimed at ocean observation; see Table 4), for the two best island events. The value of  $A_0$  is uncertain in the model. The values used for the Midway calculation plotted in Fig. 9 are 0.026, 0.004, 0.0005, and 0.0001, and for Lanai are 0.035, 0.007, 0.0005, and 0.0 in the blue, green red, and near-infrared bands, respectively (see section 4b). For Midway, when  $A_0$  is instead set to the nominal ocean values, 0.03, 0.007, 0.001, and 0.0007, the model TOA reflectances increase by about 0.001 in the blue, and less in the other bands. For Lanai, model results decrease by about 0.004 in the blue, and by less than 0.001 in the other bands, when  $A_0$  is instead set to the lower ocean spectral water-leaving reflectance measured near-coincident with the MISR overpass by MOBY at Lanai (section 3).

MODIS equivalent reflectances are calculated from

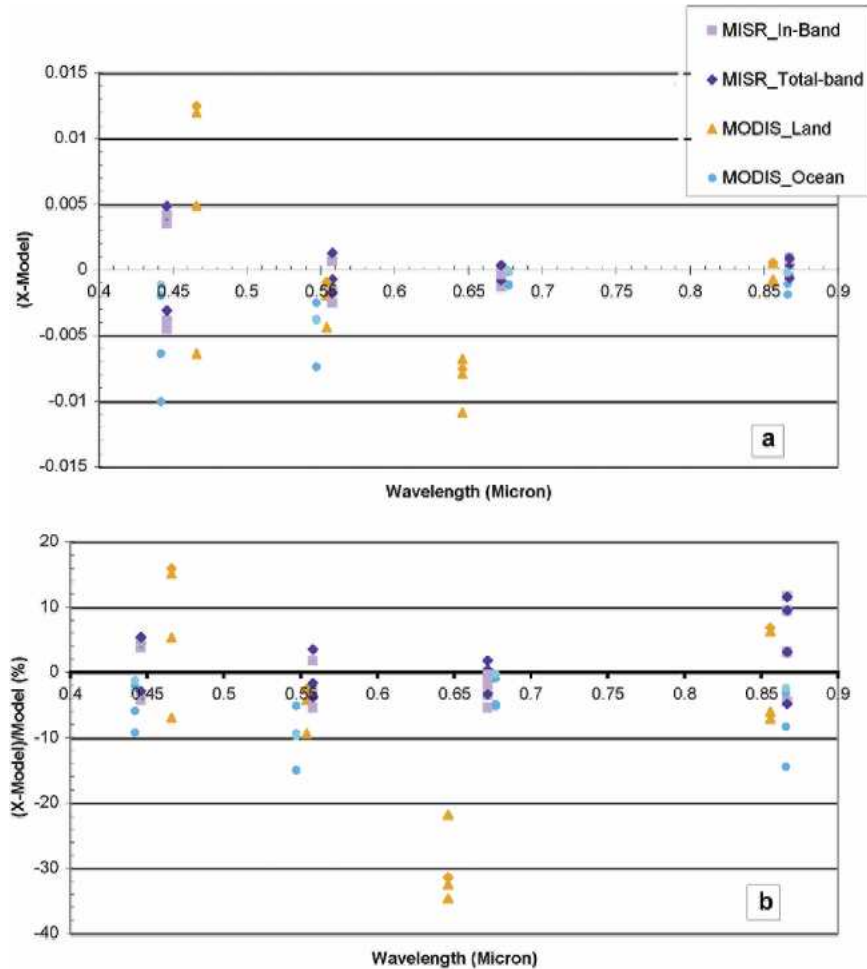


FIG. 9. (a) Absolute and (b) percent reflectance differences, for the nadir-view, MISR L1B2, version F03\_0022 product, four MODIS land channels, and four MODIS ocean channels, relative to the AERONET-constrained reference model. For the AERONET-constrained model, the  $A_0$  values used for the Midway calculation are 0.026, 0.004, 0.0005, and 0.0001, and for Lanai, they are 0.035, 0.007, 0.0005, and 0.0 in the blue, green red, and near-infrared bands, respectively. Results are shown for two patches from Lanai on 10 Feb 2002 and two patches from Midway on 9 Feb 2001.

the MODIS-02\_1KM, collection 4 standard product, according to

$$\rho_{\text{MODIS}}(\lambda) = L_{\text{MODIS}}(\lambda) \times \pi D^2 / E_0(\lambda), \quad (4)$$

where  $L_{\text{MODIS}}$  is the radiance value,  $D$  is the Earth–Sun distance in AU at the time of observation, and  $E_0$  is the band-weighted solar irradiance at TOA, for average Earth–Sun separation ( $D = 1$ ), as reported in the MODIS product and given in Table 4. For reflectance factors in the solar bands of this product, the reported uncertainty is  $\pm 2\%$  (Guenther et al. 1998). MODIS patches were collocated, to better than half a pixel, with MISR patches that meet the multiangle uniformity criterion given in section 2a. MODIS radiances were also adjusted for ozone absorption in the column, taking the

same approach as for MISR observations, but using the MODIS spectral channels.

Making precise comparisons between MISR and MODIS requires an assumption to interpolate or otherwise account for wavelength differences among the spectral bands. For Fig. 9, we began by fitting a cubic spline to the AERONET-constrained model values calculated at the four MISR effective wavelengths and used that as a spectral reflectance reference curve. We then integrated the reflectance reference curve over the MISR total bandpasses for each MISR band, and also for the in-band approximations to the bandpasses. These we designate the MISR total and in-band “model” values. Similarly, we integrated the reflectance reference curve over the MODIS land channel 3, 4, 1, and 2 bandpasses (shown in brown) and the MODIS

TABLE 4. MODIS spectral bands used.

	Effective wavelength (nm)	Effective bandwidth (nm)	$E_0^*$ ( $\text{W m}^{-2} \mu\text{m}^{-1}$ )	Spatial resolution (km)	Band type
MODIS-3	465.7	21	2089	0.5	Land
MODIS-4	553.7	21	1867.3	0.5	Land
MODIS-1	645.8	50	1606.8	0.25	Land
MODIS-2	865.1	45	993	0.25	Land
MODIS-9	442.2	11.4	1904.3	1	Ocean
MODIS-12	546.9	11.8	1893	1	Ocean
MODIS-14	676.9	13.8	1508.3	1	Ocean
MODIS-16	866.3	19	973.2	1	Ocean

\* The  $E_0$  values were obtained from the MODIS product, to assure consistent use of the MODIS calibration solar model.

ocean channel 9, 12, 14, and 16 bandpasses (shown in blue). These are the MODIS “model” values.

The reflectance differences between the MISR and MODIS measurements and their respective model values are plotted in Fig. 9a at the effective wavelength of each band, and as percent differences in Fig. 9b, for two patches from the 10 February 2002 Lanai event and two patches from the 9 February 2001 Midway event.

The scatter of points among the four patches gives an indication of the aggregated uncertainties in these comparisons; they represent the best-constrained results we can hope to obtain from this vicarious calibration effort. The MISR nadir values for all four bands straddle the zero line, scattering roughly  $\pm 5\%$  for the blue band,  $\pm 4\%$  in the green,  $\pm 2.5\%$  in the red, and  $+10\%/-2\%$  for the near-infrared, though the absolute differences for this band are comparable to those for the red (Fig. 9a). The MODIS ocean bands overlap the MISR bands in all cases and are skewed about 4% below the MISR values in the blue, green, and near-infrared wavelengths.

The MODIS land reflectances overlap the MISR nadir and MODIS ocean values in the blue, green, and near-infrared as well, falling between the MISR and MODIS ocean results in the green and near-infrared cases. But in the red spectral region, the MODIS land (band 1) reflectances are systematically lower than corresponding MISR and MODIS ocean values.

### b. Camera-to-camera comparisons

We now examine for each spectral band reflectance differences between the AERONET-constrained model and each of the nine MISR views, which we call camera-to-camera differences. There is no coincident MODIS data to compare with the off-nadir MISR cameras, so we must rely entirely on the AERONET-constrained model;  $A_0$  uncertainty remains an issue, preferentially affecting the blue and near-infrared wavelength bands and the nadir and near-nadir cameras, even if the water-leaving reflectance is Lambertian over all the geometries of interest. In the comparison overview given by Fig. 7, we adopted nominal clean ocean values for  $A_0$ . We recognized that although the band-specific camera-to-camera patterns were similar

for most cases, differences in  $A_0$  could account at least in part for the way plots for some sites are systematically displaced relative to others along the vertical axis. Since the four aft-viewing cameras have nearly the same percent discrepancy with the model in most cases, we can select event-specific  $A_0$  values for each band that come as close as possible to making the discrepancies equal. In doing this, we are in effect exploring the hypothesis that there is no systematic camera-to-camera calibration discrepancy among these cameras. For the best Midway and Lanai cases, the required  $A_0$  adjustments are small compared to the estimated uncertainties, except in the near-infrared band; the results are shown in Fig. 10.

In the blue, green, and red bands, the patches for each event are clustered to  $\pm 2\%$  or better, and the camera-to-camera pattern, though displaced, is nearly the same for the two events. The nadir-viewing (An) camera is unique, registering a discrepancy with the model between 4% and 8% smaller than the aft-viewing cameras in Fig. 10. Discrepancies for the two forward-viewing cameras not in sun glint (Df and Cf) come very close to the An camera in the blue and green bands, whereas for the red band, the discrepancy is comparable to that for the aft-viewing camera group. These patterns are also reflected in the more scattered, generally lower quality events aggregated in Fig. 7. For the largest AOT cases studied here, small aerosol-model errors can affect the vicarious calibration results in the highly sensitive, steeply viewing cameras (e.g., Fig. 8).

The camera-to-camera difference pattern arising in Fig. 10 bears some relationship to the MISR radiometric calibration process (Bruegge et al. 1996; Bruegge et al. 2004), since different components of the onboard calibration system are used for the nadir-, fore-, and aft-viewing camera groups. The absolute calibration scale is set by comparing TOA radiance, calculated based on field vicarious surface and atmospheric measurements (Abdou et al. 2002), with the response of a very stable, onboard, high-quantum-efficiency blue diode simultaneously viewing the scene. The band-to-band scale is established when the blue standard diode, and secondary diodes covering the other spectral chan-

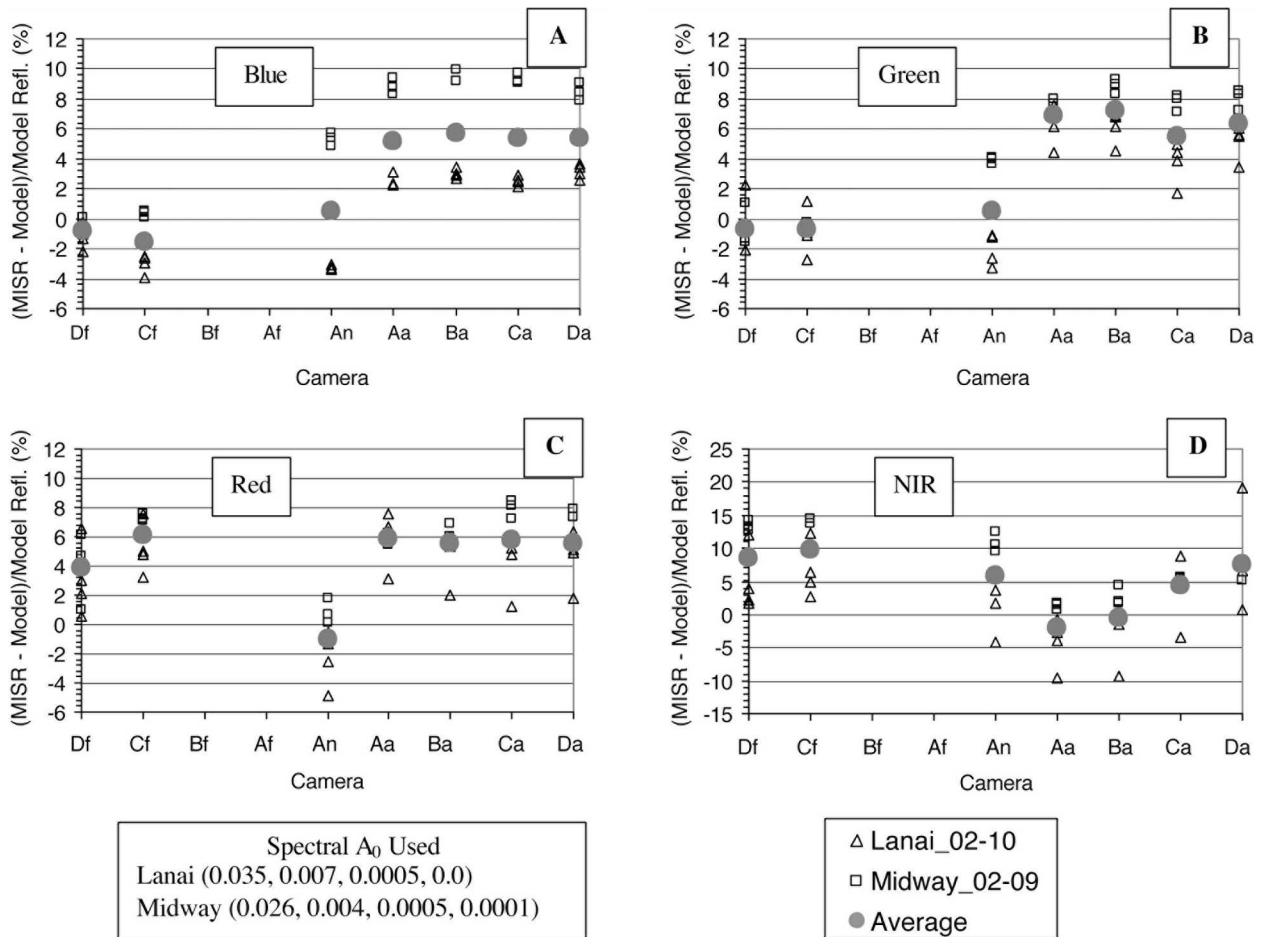


FIG. 10. Camera-to-camera differences between MISR equivalent reflectances and those calculated from the AERONET-constrained model, expressed as a percent of the model value. Results are included for four patches from Lanai on 10 Feb 2002 and three patches from Midway on 9 Feb 2001. The four plots show the MISR (a) blue, (b) green, (c) red, and (d) near-infrared spectral bands.

nels, observe deployable, sun-lit, Spectralon diffuser panels together. Diode field-of-view and solar spectrum differences are taken into account, and the panels themselves are assumed white. The individual cameras and secondary diodes then view the sun-lit panels simultaneously to complete the camera-to-camera on-board calibration. Since the cameras do not all view the panels at the same angle as the calibration diodes, panel bidirectional reflectance functions are used. These were measured prelaunch and are checked periodically by another onboard diode package mounted on a goniometer.

There are two onboard Spectralon panels: the forward-viewing camera group, along with the red and near-infrared bands of the nadir camera, is calibrated by observing the “south” panel, whereas the aft-viewing camera group and the nadir blue and green bands view the north panel. There are three sets of secondary diodes involved: one for each of the fore- and aft-viewing camera groups, and one for the nadir.

Given the repeatability of the pattern, the uncertainty in  $A_0$ , and the observed scatter from event to

event, we conclude from Fig. 10 that at low light levels, the aft-viewing cameras may be reporting too high a reflectance in the blue, green, and possibly the red, relative to the AERONET-constrained model. Better agreement is found in the nadir- and the forward-viewing cameras, especially in the blue and green. Camera-to-camera observations for the near-infrared are inconclusive.

Corroborating evidence to test these results would be helpful. Fortunately, we obtained such data during the CLAMS campaign.

### c. MISR and AirMISR observations at CLAMS

The CLAMS campaign aimed at acquiring validation data for the MISR, MODIS, and Clouds and the Earth’s Radiant Energy System (CERES) instruments aboard the EOS *Terra* satellite (Smith et al. 2005). The two MISR golden days of the campaign were 17 July and 2 August 2001. On these occasions, coincident data were taken over dark water near the Chesapeake Lighthouse by MISR and a Convair CV-580 aircraft heavily instrumented to measure atmospheric and surface

properties, including aerosol optical depth, aerosol chemistry, and ocean-surface reflectance. An AERONET sun photometer, micropulse lidar, and meteorological instruments operated on the lighthouse as well. And at the same time, AirMISR, an aircraft instrument having a single MISR camera that flies on an ER-2 aircraft at 20 km and pivots to obtain nine-angle observations similar to those from MISR (Diner et al. 1998b), observed a  $9 \text{ km} \times 11 \text{ km}$  patch within the MISR field of view, which included the lighthouse itself (see Fig. 4 of Smith et al. 2005). Unlike MISR, AirMISR is periodically calibrated in the laboratory (Chrien et al. 2001).

Figure 11 shows the MISR and AirMISR green-band reflectances for two  $3 \text{ km} \times 3 \text{ km}$  patches, one each on 17 July (Figs. 11a and 11b, for MISR and AirMISR, respectively) and 2 August (Figs. 11c and 11d). Both

patches are within a few hundred meters of the lighthouse, in cloud-free regions that meet the patch variability criterion given in section 2a. Also plotted in Fig. 11 are MISR\_RT model reflectances, constrained by AERONET AOT and aerosol size distribution taken at the lighthouse, aerosol SSA set to  $0.97 \pm 0.03$  at all wavelengths of interest, and  $A_0$  obtained from the Cloud Absorption Radiometer (CAR) instrument aboard the CV-580 (Gatebe et al. 2005). Within the AERONET-observed AOT variability, model inputs were selected to minimize AirMISR–AERONET differences; measured green-band AOT was  $0.400 \pm 0.027$  and  $0.0975 \pm 0.009$  within  $\pm 1 \text{ h}$  of the MISR overpass on 17 July and 2 August, respectively.

As with Fig. 10, the MISR aft-viewing cameras show higher reflectances, relative to the model, than the forward-viewing cameras in Fig. 11. The green-band fore-

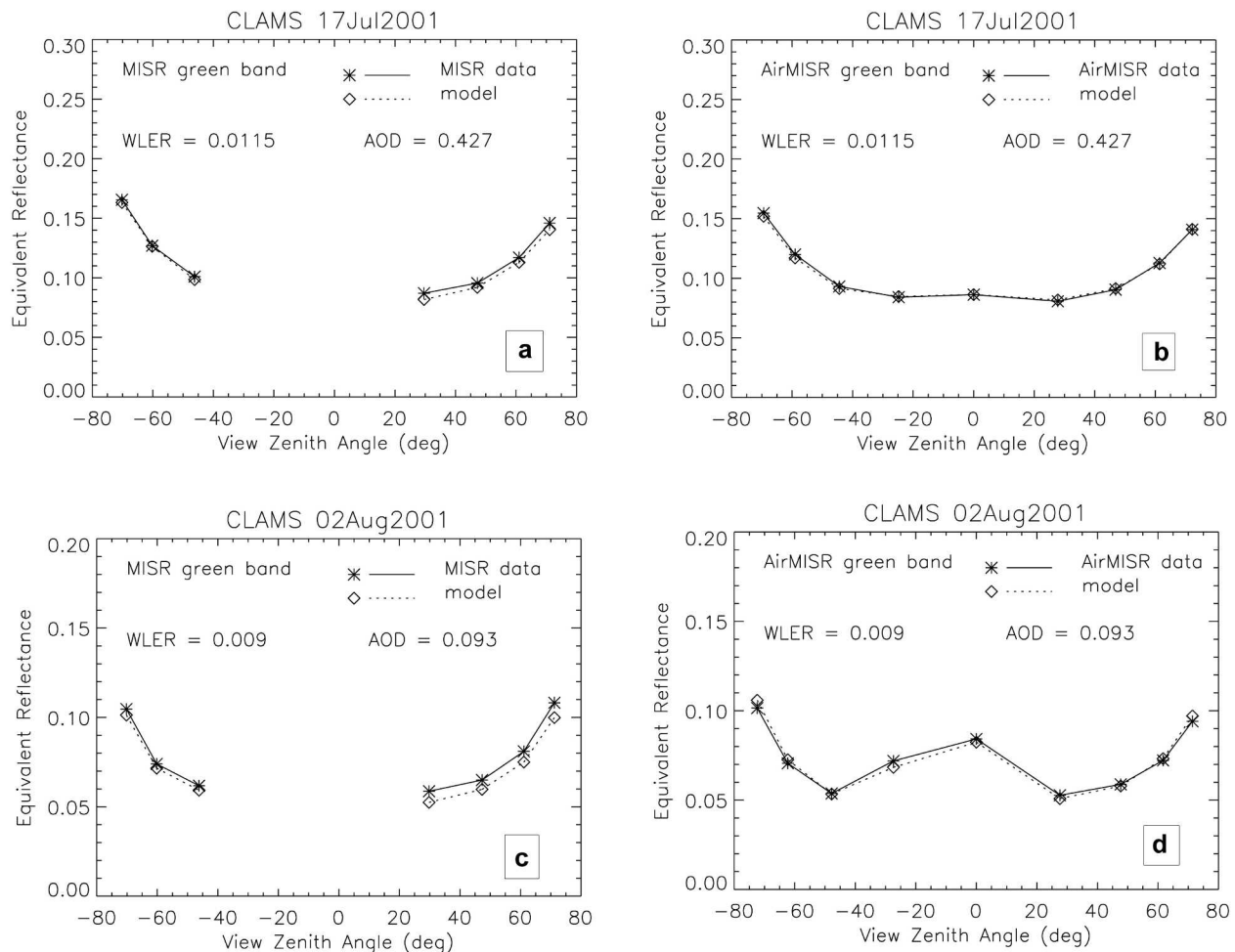


FIG. 11. MISR and AirMISR green-band reflectances, taken near the Chesapeake Lighthouse during the CLAMS campaign. MISR-RT model reflectances for (a), (b) 17 Jul and (c), (d) 2 Aug 2001, constrained by AERONET and field data, are also plotted for comparison. In this figure, the camera axes are labeled with the view zenith angle (0 for the nadir view; forward views have negative angles); for the MISR observations, glint-contaminated views are eliminated, whereas for AirMISR, the MISR-RT standard glint model is used, with a wind speed of  $4.6 \text{ m s}^{-1}$  on 17 Jul and  $3.9 \text{ m s}^{-1}$  on 2 Aug. AERONET-measured optical depth (AOD) and water-leaving reflectance (WLER) from the CAR instrument used in the model calculations are shown as text.

aft differences are near 3% and 5% for 17 July and 2 August, respectively, amounting to about 0.003 in reflectance units. Since AirMISR is a single pivoting camera, we would not expect calibration differences that depend on view angle. None are found, which lends confidence to the model and strengthens our conclusions about camera-to-camera behavior.

The MISR data are also higher than the model by a few percent in the forward-viewing cameras on both days. The discrepancy here is greater on 2 August, when the column AOT was lower, and surface contributions may be more important. One possibility is that light from bright clouds and land in the larger MISR field-of-view produce a small amount of scattered light in the camera system. A contribution of only 1.3% of the line-average reflectance would account for the discrepancy observed over the dark water; an adaptive correction is under study by the MISR team.

## 5. Conclusions

To take advantage of MISR's multiangle AOT sensitivity for low-reflectance oceanic scenes, we have pushed the limits of the vicarious calibration technique. AOT is usually well below 0.3 at midvisible wavelengths in the MISR record over ocean; typical situations produce TOA equivalent reflectances from around 0.10 in the blue to 0.02 and less in the near-infrared.

We identified high-quality, coincident MISR and AERONET observations of isolated island sites and compared reflectances derived from the standard MISR radiance product over dark water with modeled values constrained by AERONET and local meteorological data. For the nadir views, we also compared these with precisely collocated, simultaneous MODIS reflectances, and we tested the observed patterns with multiplatform coincident data taken during the CLAMS field campaign.

The nominal 5% MISR low-light-level calibration accuracy (Bruegge et al. 2004) falls within the formal uncertainties of this work, but consistency among many events, involving different sites, AERONET sun photometers, and environmental conditions, and spanning the MISR mission, builds confidence in the absolute, band-to-band, and camera-to-camera calibration patterns that emerge. Conclusions are strongest in the red and green bands. The blue band is affected by uncertainty in water-leaving reflectance ( $A_0$ ). For the near-infrared band, the results of this study are inconclusive because of low absolute reflectance and extreme sensitivity to any errors in surface and aerosol properties.

For the best-constrained events, MODIS ocean-band reflectances are skewed about 4% below the MISR values in the blue, green, and near-infrared spectral regions. Bruegge et al. (2004) found that MISR and MODIS absolute calibration differed by 3% in the same sense at higher reflectance levels ( $\sim 0.3$ ) and

traced the discrepancy to the MISR team's selection of field vicarious calibration versus the MODIS team's choice of their onboard calibrator as absolute radiometric calibration standards.

The MODIS land-band reflectances overlap the MISR nadir and MODIS ocean values in the blue, green, and near-infrared as well, falling between the MISR and MODIS ocean results in the green and near-infrared cases. But in the red spectral region, the MODIS band 1 reflectances are systematically lower than the corresponding MISR and MODIS ocean-band values.

At low light levels, camera-to-camera comparisons with the AERONET-constrained model exhibit a persistent pattern: the MISR aft-viewing cameras report reflectances too high by several percent in the blue, green, and possibly the red, relative to the model. Better agreement is found in the nadir- and the forward-viewing cameras, especially in the blue and green.

Figure 12 shows the cumulative effect on retrieved AOT of correcting for the camera-to-camera effects indicated in section 4, plus a MISR spectral calibration adjustment (Bruegge et al. 2004), made in part based on an early version of Fig. 9. The spectral correction reduces the red-band reflectance by 3% and the near-infrared by 1%, in all cameras, and leaves the other bands unchanged. It is applied to version 22 and higher of the MISR level 1B2 radiance product, which includes all MISR data shown in this paper except the "uncorrected" data in Fig. 12. (One consequence of making this correction is the unbiased scatter of MISR reflectances appearing in Fig. 9.) The camera-to-camera adjustment made amounts to a reduction of 1%–2% in the aft-viewing cameras, about 1% in the Bf camera, and an increase of order 0.5% in the Df and Cf, leaving the Af and An cameras unchanged. These calibration adjustments decrease the MISR-retrieved green-band AOT by about 0.02, on average, for the 910 dark water cases plotted in Fig. 12, reducing by about 40% the average AOT discrepancy relative to sun-photometer values for dark water sites (Redemann et al. 2005; Kahn et al. 2004). The adjustments applied here do not include any absolute or stray-light corrections, which are still under study and would reduce the differences further.

The MISR team is pursuing additional calibration exercises, aimed at independently testing sensor response over the full range of light levels, including 1) vicarious calibration from MISR lunar images, 2) fore-aft camera reflectance comparisons for observations having symmetric scattering geometries, 3) postlaunch, high-precision laboratory characterization of a prototype MISR camera, and 4) MISR–CERES statistical albedo comparisons over the full range of light levels. Refinement of the MISR calibration based on a synthesis of these studies, along with the results of the present work, amount to adjustments of no more than a few percent. It will be reported in a subsequent paper,

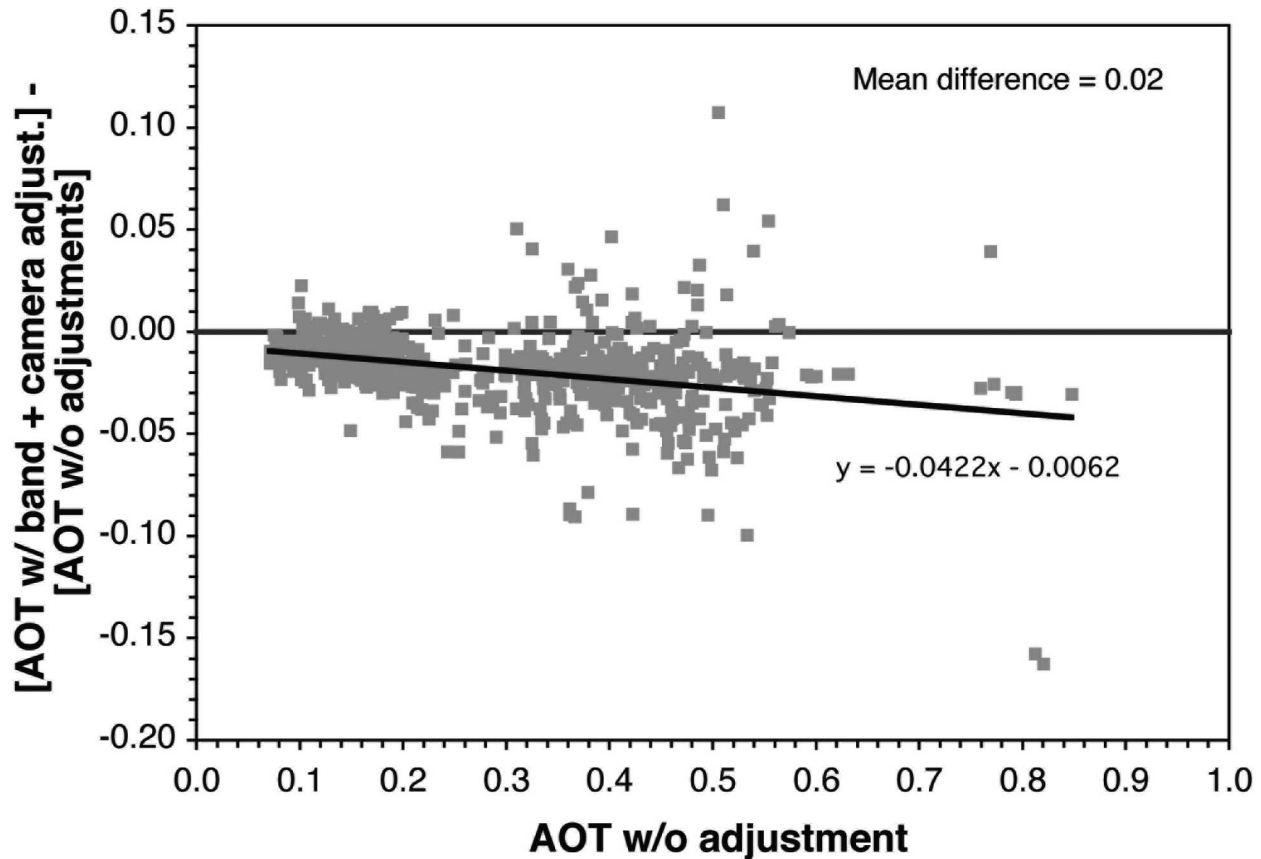


FIG. 12. Differences between green-band AOT retrieved using the MISR standard aerosol algorithm with and without spectral and camera-to-camera calibration adjustments, plotted against the uncorrected green-band AOT. This figure contains 910 globally distributed points over dark water sites, obtained during Mar 2002.

and any changes will be implemented in reprocessed MISR level 1B2 radiance and MISR level 2AS aerosol-surface products.

For future spacecraft instruments designed to retrieve aerosol properties over dark water, we conclude that calibration should be given special attention, particularly at low light levels, using complementary preflight and onboard calibration schemes, along with vicarious comparisons, to reduce the uncertainties even further.

Factors in addition to calibration affect the quality of aerosol retrievals over dark water, such as the range of aerosol-model microphysical properties assumed in the retrieval algorithm, treatment of the ocean-surface boundary condition, and scene variability over the instrument sampling region (e.g., Kahn et al. 2004). These are the subjects of continuing study by the MISR Team.

*Acknowledgments.* We thank the MISR Calibration Team for their diligence at characterizing and assessing the MISR preflight, onboard, and field vicarious calibration programs, and Nadine Chrien, Michael Gunson, Earl Hansen, Skye Knighton, Kyle Miller, and Cinzia Zuffada for their support of these efforts. We also

thank Jack Xiong of the MODIS Calibration Team for detailed discussion of Fig. 9. The work presented here is funded in part by the EOS-MISR instrument program, and by the Climate and Radiation Research and Analysis Program in the Earth Sciences Division of the National Aeronautics and Space Administration, under D. Anderson and H. Maring. This work is performed at the Jet Propulsion Laboratory, California Institute of Technology, under contract with NASA.

#### REFERENCES

- Abdou, W. A., C. J. Bruegge, M. C. Helmlinger, J. E. Conel, S. H. Pilorz, W. C. Ledebner, B. J. Gaitley, and K. J. Thome, 2002: Vicarious calibration experiment in support of the Multi-angle Imaging SpectroRadiometer. *IEEE Trans. Geosci. Remote Sens.*, **40**, 1500–1511.
- , and Coauthors, 2005: Comparison of coincident MISR and MODIS aerosol optical depths over land and ocean scenes containing AERONET sites. *J. Geophys. Res.*, in press.
- Bruegge, C. J., D. J. Diner, and V. G. Duval, 1996: The MISR calibration program. *J. Atmos. Oceanic Technol.*, **13**, 286–299.
- , V. G. Duval, N. L. Chrien, R. P. Korechoff, B. J. Gaitley, and E. B. Hochberg, 1998: MISR prelaunch instrument calibration and characterization results. *IEEE Trans. Geosci. Remote Sens.*, **36**, 1186–1198.

- , N. L. Chrien, R. R. Ando, D. J. Diner, W. A. Abdou, M. C. Helmlinger, S. H. Pilorz, and K. J. Thome, 2002: Early validation of the Multi-angle Imaging SpectroRadiometer (MISR) Radiometric Scale. *IEEE Trans. Geosci. Remote Sens.*, **40**, 1477–1492.
- , W. A. Abdou, D. J. Diner, B. J. Gaitley, M. C. Helmlinger, R. A. Kahn, and J. V. Martonchik, 2004: Validating of the MISR radiometric scale for the ocean aerosol science communities. *Post-Launch Calibration of Satellite Sensors*, S. A. Morain and A. M. Budge, Eds., A. A. Balkema, 103–115.
- Chrien, N. L., C. J. Bruegge, and B. J. Gaitley, 2001: AirMISR laboratory calibration and inflight performance results. *Remote Sens. Environ.*, **77**, 328–337.
- , —, and R. R. Ando, 2002: Multi-angle Imaging Spectro-Radiometer (MISR) On-Board Calibrator (OBC) In-flight Performance Studies. *IEEE Trans. Geosci. Remote Sens.*, **40**, 1493–1499.
- Clark, D. K., H. R. Gordon, K. J. Voss, Y. Ge, W. Broenkow, and C. Trees, 1997: Validation of atmospheric correction over the ocean. *J. Geophys. Res.*, **102**, 17 209–17 217.
- Clarke, A. D., W. G. Colling, P. J. Rasch, V. N. Kapustin, K. Moore, S. Howell, and H. E. Fuelberg, 2001: Dust and pollution transport on global scales: Aerosol measurements and model predictions. *J. Geophys. Res.*, **106**, 32 555–32 569.
- Diner, D. J., and Coauthors, 1998a: Multi-angle Imaging Spectro-Radiometer (MISR) description and experiment overview. *IEEE Trans. Geosci. Remote Sens.*, **36**, 1072–1087.
- , and Coauthors, 1998b: The Airborne Multi-angle Imaging SpectroRadiometer (AirMISR): Instrument description and first results. *IEEE Trans. Geosci. Remote Sens.*, **36**, 1339–1349.
- Dubovik, O., and M. D. King, 2000: A flexible inversion algorithm for retrieval of aerosol optical properties from sun and sky radiance measurements. *J. Geophys. Res.*, **105**, 20 673–20 696.
- , A. Smirnov, B. N. Holben, M. D. King, Y. J. Kaufman, T. F. Eck, and I. Slutsker, 2000: Accuracy assessments of aerosol optical properties retrieved from Aerosol Robotic Network (AERONET) sun and sky radiance measurements. *J. Geophys. Res.*, **105**, 9791–9806.
- , B. Holben, T. F. Eck, A. Smirnov, Y. J. Kaufman, M. E. King, D. Tanre, and I. Slutsker, 2002: Variability of absorption and optical properties of key aerosol types observed in worldwide locations. *J. Atmos. Sci.*, **59**, 590–608.
- Gao, Y., Y. J. Kaufman, D. Tanre, D. Kolber, and P. G. Falkowski, 2001: Seasonal distributions of aeolian iron fluxes to the global ocean. *Geophys. Res. Lett.*, **28**, 29–32.
- Gatebe, C. K., M. D. King, A. I. Lyapustin, G. T. Arnold, and J. Redemann, 2005: Airborne spectral measurements of ocean directional reflectance. *J. Atmos. Sci.*, **62**, 1072–1092.
- Guenther, B., G. D. Godden, X. Xiong, E. J. Knight, H. Montgomery, M. M. Hopkins, M. G. Khayat, and Z. Hao, 1998: Pre-launch algorithm and data format for the level 1 calibration products for the EOS AM-1 Moderate Resolution Imaging Spectroradiometer (MODIS). *IEEE Trans. Geosci. Remote Sens.*, **36**, 1142–1151.
- Holben, B. N., and Coauthors, 1998: AERONET—A federated instrument network and data archive for aerosol characterization. *Remote Sens. Environ.*, **66**, 1–16.
- Husar, R. B., J. M. Prospero, and L. L. Stowe, 1997: Characterization of tropospheric aerosols over ocean with the NOAA Advanced Very High Resolution Radiometer optical thickness operational product. *J. Geophys. Res.*, **102**, 16 889–16 909.
- Jin, Z., T. P. Charlock, and K. Rutledge, 2002: Analysis of broadband solar radiation and albedo over the ocean surface at COVE. *J. Atmos. Oceanic Technol.*, **19**, 1585–1601.
- Jovanovic, V. M., M. A. Bull, M. M. Smyth, and J. Zong, 2002: MISR in-flight camera geometric model calibration and georectification performance. *IEEE Trans. Geosci. Remote Sens.*, **40**, 1512–1519.
- Kahn, R., P. Banerjee, D. McDonald, and D. J. Diner, 1998: Sensitivity of multiangle imaging to aerosol optical depth and to pure-particle size distribution and composition over ocean. *J. Geophys. Res.*, **103**, 32 195–32 213.
- , —, and —, 2001a: The sensitivity of multiangle imaging to natural mixtures of aerosols over ocean. *J. Geophys. Res.*, **106**, 18 219–18 238.
- , —, —, and J. Martonchik, 2001b: Aerosol properties derived from aircraft multiangle imaging over Monterey Bay. *J. Geophys. Res.*, **106**, 11 977–11 995.
- , B. J. Gaitley, J. V. Martonchik, D. J. Diner, K. A. Crean, and B. Holben, 2005: MISR global aerosol optical depth validation based on two years of coincident AERONET observations. *J. Geophys. Res.*, in press.
- Kalashnikova, O. V., R. Kahn, I. N. Sokolik, and W.-H. Li, 2005: The ability of multi-angle remote sensing observations to identify and distinguish mineral dust types: Part 1. Optical models and retrievals of optically thick plumes. *J. Geophys. Res.*, in press.
- Koepke, P., 1984: Effective reflectance of oceanic whitecaps. *Appl. Opt.*, **23**, 1816–1824.
- Martonchik, J. V., D. J. Diner, R. Kahn, M. M. Verstraete, B. Pinty, H. R. Gordon, and T. P. Ackerman, 1998: Techniques for the retrieval of aerosol properties over land and ocean using multiangle imaging. *IEEE Trans. Geosci. Remote Sens.*, **36**, 1212–1227.
- , —, —, B. J. Gaitley, and B. N. Holben, 2004: Comparison of MISR and AERONET aerosol optical depths over desert sites. *Geophys. Res. Lett.*, **31**, L16102, doi:10.1029/GL019807.
- Monahan, E. C., and I. O. Muirchearthaigh, 1980: Optimal power-law description of oceanic whitecap coverage dependence on wind speed. *J. Phys. Oceanogr.*, **10**, 2094–2099.
- Morel, A., and S. Maritorena, 2001: Bio-optical properties of oceanic waters: A reappraisal. *J. Geophys. Res.*, **106**, 7163–7180.
- Penner, J. E., and Coauthors, 1994: Quantifying and minimizing uncertainty of climate forcing by anthropogenic aerosols. *Bull. Amer. Meteor. Soc.*, **75**, 375–400.
- Prospero, J. M., R. J. Charlson, V. Mohnen, R. Jaenicke, A. C. Delany, J. Moyers, W. Zoller, and K. Rahn, 1983: The atmospheric aerosol system: An overview. *Rev. Geophys. Space Phys.*, **21**, 1607–1629.
- Redemann, J., and Coauthors, 2005: Suborbital measurements of spectral aerosol optical depth and its variability at subsatellite grid scales in support of CLAMS 2001. *J. Atmos. Sci.*, **62**, 993–1007.
- Shettle, E. P., and R. W. Fenn, 1979: Models for the aerosols of the lower atmosphere and the effects of humidity variations on their optical properties. Environmental Research Papers AFGL-TR-79-0214, Air Force Geophysics Laboratory, 94 pp.
- Smirnov, A., B. N. Holben, T. F. Eck, O. Dubovik, and I. Slutsker, 2000: Cloud screening and quality control algorithms for the AERONET database. *Remote Sens. Environ.*, **73**, 337–349.
- , —, Y. J. Kaufman, O. Dubovik, T. F. Eck, I. Slutsker, C. Pietras, and R. N. Halthore, 2002: Optical properties of atmospheric aerosol in maritime environments. *J. Atmos. Sci.*, **59**, 501–523.
- , —, O. Dubovik, R. Frouin, T. F. Eck, and I. Slutsker, 2003: Maritime component in aerosol optical models derived from Aerosol Robotic Network data. *J. Geophys. Res.*, **108**, 4033, doi:10.1029/2002JD002701.
- Smith, W. L., Jr., T. P. Charlock, R. Kahn, J. V. Martins, and L. Remer, 2005: EOS-Terra aerosol and radiative flux validation: An overview of the Chesapeake Lighthouse and Aircraft Measurements for Satellites experiment. *J. Atmos. Sci.*, **62**, 903–918.
- Yang, H., and H. R. Gordon, 1997: Remote sensing of ocean color: Assessment of water-leaving radiance bidirectional effects on atmospheric diffuse transmittance. *Appl. Opt.*, **36**, 7887–7897.